FRONTIERS OF PHYSICS

RESEARCH ARTICLE
Volume 19 / Issue 2 / 22203 / 2024

Fast nuclear-spin gates and electrons–nuclei entanglement of neutral atoms in weak magnetic fields

Xiao-Feng Shi

School of Physics, Xidian University, Xi'an 710071, China
Corresponding author. E-mail: shixiaofeng@xidian.edu.cn
Received December 20, 2022; accepted June 21, 2023

ABSTRACT

We present a novel class of Rydberg-mediated nuclear-spin entanglement in divalent atoms with global laser pulses. First, we show a fast nuclear-spin controlled phase gate of an arbitrary phase realizable either with two laser pulses when assisted by Stark shifts, or with three pulses. Second, we propose to create an electrons–nuclei-entangled state, which is named a super bell state (SBS) for it mimics a *large* Bell state incorporating three *small* Bell states. Third, we show a protocol to create a three-atom electrons-nuclei entangled state which contains the three-body *W* and Greenberger–Horne–Zeilinger (GHZ) states simultaneously. These protocols possess high intrinsic fidelities, do not require single-site Rydberg addressing, and can be executed with large Rydberg Rabi frequencies in a weak, Gauss-scale magnetic field. The latter two protocols can enable measurement-based preparation of Bell, hyperentangled, and GHZ states, and, specifically, SBS can enable quantum dense coding where one can share three classical bits of information by sending one particle.

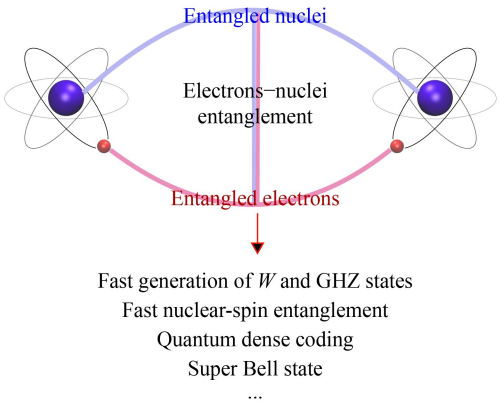

Keywords nuclear-spin qubit, electrons–nuclei entanglement, super Bell state, Greenberger–Horne–Zeilinger state, Rydberg-mediated entanglement, quantum dense coding

1 Introduction

Rydberg-mediated entanglement [1, 2] with individual alkali-metal atoms was extensively explored experimentally in the last fourteen years [3–18]. Recently, people demonstrated Rydberg-mediated entanglement in alkaline-earth-like (AEL) atoms, such as ytterbium and strontium [19–23]. Compared to alkali-metal atoms, divalent AEL atoms of the alkaline-earth-metal, lanthanide, or transition-metal species can be easily cooled to low temperatures [19, 24–28] and long-lived trapping of both the ground and Rydberg states is realizable [29]. A special advantage in AEL is that for isotopes with nuclear spins, quantum information stored in nuclear spin states [30, 31] is insensitive to magnetic noise, can be preserved during laser cooling [32, 33], and one neutral atom can host multiple, stable, and controllable nuclear-spin states useful for coding information [31, 34, 35]. But concerning entanglement, no protocols were designed specifically for nuclear spins that exhibit a privilege for nuclear-spin qubits in AEL atoms.

In this paper, we study a class of nuclear-spin entanglement enabled by a novel mechanism for creating unit Rydberg excitation in multiple atoms solely applicable for AEL atoms with nuclear spins. We show protocols to generate two-atom nuclear-spin entanglement that can be executed exceedingly fast, and present protocols for creating two- and three-atom electrons–nuclei entanglement. We further show that the electrons–nuclei entangled state can be used for measurement-based creation of W

Higher Education Press

arXiv: 2212.05876
https://doi.org/10.1007/s11467-023-1332-0

and Greenberger–Horne–Zeilinger (GHZ) states, and can enable quantum dense coding in which three classical bits of information can be securely shared when only one particle is sent in a public channel. These reveal nuclear-spin-possessing AEL atoms as a versatile platform for exploring functional quantum devices.

1.1 Fast nuclear-spin entanglement

In AEL atoms with nuclear spins, the g-factors of the ground and clock states are mainly of nuclear-spin character [36] which can lead to simultaneous Rydberg excitation of both nuclear-spin qubit states [37]. A useful protocol of entanglement generation is simultaneously exciting one out of the two qubit states in each atom to Rydberg states [11, 18, 38], which means that the other qubit state in each atom is not Rydberg excited. To employ this method with nuclear-spin qubits, one can choose a Rydberg Rabi frequency Ω small compared to the Zeeman splitting Δ_Z in the Rydberg states [20, 23, 35], or use selection rules [37]. Nonetheless, for nuclear spin qubits defined in the clock state, sizable UV-laser Rydberg Rabi frequencies Ω can be realized [19, 22, 35] which seems an advantage, but the selection-rule method of [37] cannot work for the clock-Rydberg transition, and using $\Omega \ll \Delta_Z$ (e.g., the experiments in Refs. [20, 23] had $\Omega/\Delta_Z < 0.17$) would either lengthen the gate duration with Gauss-scale B-fields or bring extra magnetic noise when strong B-fields are used.

Here, we present nuclear-spin entangling gates realizable with a large Ω in a weak magnetic field when $\Omega/\Delta_Z \lessapprox 1$. By exciting the four nuclear spin qubit states in two atoms simultaneously from the ground or clock state to Rydberg states, a two-qubit controlled phase gate of an arbitrary phase is realizable with three laser pulses of total duration about $5.05\pi/\Omega_m$, or with two pulses of total duration about $2.59\pi/\Omega_m$ when assisted by Stark shift, where Ω_m is the maximal Rabi frequency in the pulses. With Ω_m over $2\pi \times 6$ MHz [19, 22, 35], the gate duration can be less than $0.42(0.22)$ μs for the three (two)-pulse gate, or even shorter for clock-Rydberg Rabi frequencies over $2\pi \times 10$ MHz are realizable [19]. Importantly, the gates are compatible with Gauss-scale magnetic fields as in recent nuclear-spin-qubit experiments [20, 23, 39, 40].

1.2 A super Bell state

The nuclear-spin states in both the ground and metastable clock states of AEL atoms can enable a novel entanglement, namely, a simultaneous entanglement between two atoms in the external space, and entanglement between the electrons and nuclei. However, it was not reported how such states can be prepared.

In this paper, we present a three-pulse protocol to realize the following state entangled between the electrons (e) and nuclear spins (n) in two atoms via Rydberg blockade,

$$|SB\rangle \equiv \frac{1}{\sqrt{2}}\left(|\mathrm{cc}\rangle_\mathrm{e} \otimes |\Phi\rangle_\mathrm{n} + |\Phi\rangle_\mathrm{e} \otimes |\Psi\rangle_\mathrm{n}\right), \tag{1}$$

where

$$|\Phi\rangle_\mathrm{n} = \frac{|{\uparrow\downarrow}\rangle_\mathrm{n} + |{\downarrow\uparrow}\rangle_\mathrm{n}}{\sqrt{2}},$$
$$|\Psi\rangle_\mathrm{n} = \frac{\mathrm{e}^{\mathrm{i}\theta}|{\uparrow\uparrow}\rangle_\mathrm{n} + \mathrm{e}^{\mathrm{i}\theta'}|{\downarrow\downarrow}\rangle_\mathrm{n}}{\sqrt{2}} \tag{2}$$

are two orthogonal Bell states entangled in the two nuclear spin states $\uparrow$ and $\downarrow$, θ and θ' are two angles, and

$$|\Phi\rangle_\mathrm{e} = \frac{|\mathrm{cg}\rangle_\mathrm{e} + |\mathrm{gc}\rangle_\mathrm{e}}{\sqrt{2}}$$

is a Bell state entangled in the electronic ground (g) and clock (c) states. Because of the similar structure, $|\Phi\rangle_\mathrm{n}$ and $|\Phi\rangle_\mathrm{e}$ are labeled by the same Greek letter. Looking at it as a whole, Eq. (1) is entangled between the two-atom electronic states $(|\mathrm{cc}\rangle_\mathrm{e}, |\Phi\rangle_\mathrm{e})$ and the two-atom nuclear spin states $(|\Phi\rangle_\mathrm{n}, |\Psi\rangle_\mathrm{n})$. For want of a better term, Eq. (1) is called a supper Bell state (SBS) because it is like a large Bell state including three "small" Bell states. To our knowledge, no such exotic two-particle entangled state containing three Bell states was reported.

SBS is prepared by three laser pulses, two UV laser pulses for the clock-Rydberg transition and one laser pulse for the ground-Rydberg transition. The three pulses have a total duration $3.4\pi/\Omega_\mathrm{eff}$ (or $7.7\pi/\Omega$), where Ω_eff is the Rabi frequency for the ground-Rydberg transition and Ω is the largest UV laser Rabi frequency among the two UV laser pulses for the clock-Rydberg transition.

SBS can enable quantum dense coding [41]. By sending one of the two particles in the state of SBS, three bits of information can be shared as shown in Section 7.

1.3 A three-atom state including W and GHZ states

Our theory can be used to realize the following state

$$|\blacktriangle\rangle = \frac{1}{2}\left[(\sqrt{3}|\mathrm{ccc}\rangle_\mathrm{e} \otimes \cancel{H}\rangle_\mathrm{n} + |W\rangle_\mathrm{e} \otimes |\mathrm{GHZ}\rangle_\mathrm{n})\right], \tag{3}$$

which has rich entanglement in three atoms, where

$$|\cancel{H}\rangle_\mathrm{n} = \frac{1}{\sqrt{6}}\Big[|{\uparrow\uparrow\downarrow}\rangle_\mathrm{n} + |{\uparrow\downarrow\uparrow}\rangle_\mathrm{n} + |{\downarrow\uparrow\uparrow}\rangle_\mathrm{n} + \mathrm{e}^{\mathrm{i}\Theta}(|{\uparrow\downarrow\downarrow}\rangle_\mathrm{n} + |{\downarrow\uparrow\downarrow}\rangle_\mathrm{n} + |{\downarrow\downarrow\uparrow}\rangle_\mathrm{n})\Big]$$

is the sum of two different nuclear-spin W states with a relative phase Θ,

$$|W\rangle_\mathrm{e} = \frac{1}{\sqrt{3}}\left(|\mathrm{gcc}\rangle_\mathrm{e} + |\mathrm{cgc}\rangle_\mathrm{e} + |\mathrm{ccg}\rangle_\mathrm{e}\right)$$

is an electronic W state [42, 43] which is maximally entangled in the ground-clock state space, and

$$|\mathrm{GHZ}\rangle_\mathrm{n} = \frac{1}{\sqrt{2}}\left(|\uparrow\uparrow\uparrow\rangle_\mathrm{n} + |\downarrow\downarrow\downarrow\rangle_\mathrm{n}\right)$$

is a Greenberger–Horne–Zeilinger (GHZ) state [44] which is maximally entangled in the nuclear-spin state space.

Like SBS, the state in Eq. (3) can be prepared by two UV laser pulses for the clock-Rydberg transition and one laser pulse for the ground-Rydberg transition with a total duration $3.5\pi/\Omega_\mathrm{eff}$ (or $11\pi/\Omega$). Because Ω_eff is in general small [37], the speed for creating $|SB\rangle$ and $|\blacktriangle\rangle$ is bottlenecked by the available laser powers for realizing the ground-Rydberg transition.

The remainder of this paper is organized as follows. In Section 2, we study a three-pulse protocol to realize a quantum gate in the nuclear spins of the clock or ground states. In Section 3, we study a similar nuclear-spin quantum gate realized by two laser pulses when assisted by Stark shift. In Section 4, we show a three-pulse protocol to create SBS. In Section 5, we show a three-pulse protocol to create a three-atom state which contains W and GHZ states simultaneously. In Section 6, we discuss creation of Bell, hyperentangled, and GHZ states by measuring the states studied in Sections 4 and 5. In Section 7, we show quantum dense coding with SBS. Sections 8 and 9 give discussions and conclusions, respectively.

2 Fast nuclear-spin quantum gates

2.1 A controlled-phase gate of any desired phase

We first show a sequence to realize a nuclear-spin quantum gate of the form,

$$\begin{aligned}
&|\mathrm{c}_\uparrow\mathrm{c}_\uparrow\rangle \rightarrowtail \mathrm{e}^{-\mathrm{i}\alpha}|\mathrm{c}_\uparrow\mathrm{c}_\uparrow\rangle,\\
&|\mathrm{c}_\uparrow\mathrm{c}_\downarrow\rangle \rightarrowtail \mathrm{e}^{-\mathrm{i}\beta/2}|\mathrm{c}_\uparrow\mathrm{c}_\downarrow\rangle,\\
&|\mathrm{c}_\downarrow\mathrm{c}_\uparrow\rangle \rightarrowtail \mathrm{e}^{-\mathrm{i}\beta/2}|\mathrm{c}_\downarrow\mathrm{c}_\uparrow\rangle,\\
&|\mathrm{c}_\downarrow\mathrm{c}_\downarrow\rangle \rightarrowtail \mathrm{e}^{\mathrm{i}\alpha}|\mathrm{c}_\downarrow\mathrm{c}_\downarrow\rangle,
\end{aligned} \tag{4}$$

where the first (second) $\mathrm{c}_{\uparrow(\downarrow)}$ represents the state of the first (second) atom, α and β are angles where β is determined by a global laser phase, and

$$\begin{aligned}
&|\mathrm{c}_\uparrow\rangle \equiv |\mathrm{c}\rangle_\mathrm{e}\otimes|\uparrow\rangle_\mathrm{n},\\
&|\mathrm{c}_\downarrow\rangle \equiv |\mathrm{c}\rangle_\mathrm{e}\otimes|\downarrow\rangle_\mathrm{n},\\
&|\mathrm{g}_\uparrow\rangle \equiv |\mathrm{g}\rangle_\mathrm{e}\otimes|\uparrow\rangle_\mathrm{n},\\
&|\mathrm{g}_\downarrow\rangle \equiv |\mathrm{g}\rangle_\mathrm{e}\otimes|\downarrow\rangle_\mathrm{n},
\end{aligned}$$

where e (n) denotes the electronic (nuclear spin) state of the atom, $\otimes$ is used because to a good approximation, the electron and nuclear spin are decoupled in both the ground (g) and clock (c) states [35, 37, 45]. The gate in Eq. (4) is a controlled-phase gate because by using the single-qubit phase gates

$$\begin{aligned}
&|\mathrm{c}_\uparrow\rangle \rightarrowtail \mathrm{e}^{\mathrm{i}\alpha/2}|\mathrm{c}_\uparrow\rangle,\\
&|\mathrm{c}_\downarrow\rangle \rightarrowtail \mathrm{e}^{\mathrm{i}(\beta-\alpha)/2}|\mathrm{c}_\downarrow\rangle,
\end{aligned}$$

in both atoms [37, 45], the gate in Eq. (4) becomes

$$\begin{aligned}
&|\mathrm{c}_\uparrow\mathrm{c}_\uparrow\rangle \rightarrowtail |\mathrm{c}_\uparrow\mathrm{c}_\uparrow\rangle,\\
&|\mathrm{c}_\uparrow\mathrm{c}_\downarrow\rangle \rightarrowtail |\mathrm{c}_\uparrow\mathrm{c}_\downarrow\rangle,\\
&|\mathrm{c}_\downarrow\mathrm{c}_\uparrow\rangle \rightarrowtail |\mathrm{c}_\downarrow\mathrm{c}_\uparrow\rangle,\\
&|\mathrm{c}_\downarrow\mathrm{c}_\downarrow\rangle \rightarrowtail \mathrm{e}^{\mathrm{i}\beta}|\mathrm{c}_\downarrow\mathrm{c}_\downarrow\rangle,
\end{aligned} \tag{5}$$

where β is adjustable by varying laser phases. The case $\beta=\pi$ corresponds to the canonical CZ gate as realized in the Rydberg quantum gate [46]. In principle, protocols used in alkali-metal atoms [47] can also be used for creating the gate in Eq. (5). But for nuclear spins in AEL, two nearby nuclear spin states in either the ground or clock states are nearly degenerate in a weak B-field, so that both nuclear spin qubit states can be excited to Rydberg states [37]. To use protocols tested with alkali-metal atomic hyperfine qubits for entangling AEL nuclear-spin qubits, one may use strong magnetic fields to suppress the Rydberg excitation of the nontarget nuclear spin states [35]. The benefit of using strong magnetic fields is that the polarization of the laser fields can fluctuate without decreasing the gate fidelity too much [35]. On the other hand, strong magnetic fields can lead to large field fluctuation in an array of atoms. A compromise is to use quite small Rydberg Rabi frequency when a weak magnetic field is employed, as in the experiments reported in Refs. [20, 23]. This raises a question whether fast nuclear-spin quantum gates can be created in a weak magnetic field. Below, we first show the physical possibility for our gate protocols and then show a gate realizable with large Rydberg Rabi frequencies in a weak magnetic field.

2.2 Laser excitation of the ground-Rydberg and clock-Rydberg transitions

The gate protocols in this paper depend on exciting the ground and clock states to Rydberg states with MHz-scale Rabi frequencies, for which we analyze in detail below.

The ground state can be excited to a $(6s6n)\,^3S_1$ Rydberg state via the largely detuned $(6s6p)\,^3P_1$ state as theoretically analyzed [37] and experimentally verified [20, 48]. The hyperfine interaction can mix the singlet and triplet states [49], but for the $F=I+1=3/2$ state there is no mixing [50]. In this paper, we consider exciting the ground or clock states to the $F=I+1$ manifold of $(6s6n)\,^3S_1$ state with $n\sim 70$, for which the nearby Rydberg states (of different F) are separated by more than 1 GHz [37], which is orders of magnitude larger

than the Rydberg Rabi frequency Ω considered in this paper. So, we can ignore the excitation of the nearby Rydberg states. Reference [37] showed that a ground-Rydberg Rabi frequency $2\pi \times 1.4$ MHz can be realized for a Rydberg state of principal quantum 70. As for the clock state, the experiment of Ref. [19] excited the clock state of strontium to a Rydberg state of $n = 61$ with a Rabi frequency up to $2\pi \times 13$ MHz, and large Rabi frequencies were possible as shown in detailed analyses [35].

We consider a Gauss-scale magnetic field for specifying the quantization axis, so that the two Zeeman substates $|\uparrow\rangle \equiv |m_I = 1/2\rangle$ and $|\downarrow\rangle \equiv |m_I = -1/2\rangle$ in the ground (or clock) state can be assumed degenerate [37]. In the $F = 3/2$ level of the $(6s6n)\,^3S_1$ Rydberg state, there is a frequency separation $2\Delta \approx 2\pi \times 1.9B$ MHz/G [35] between the two hyperfine substates $|r_\pm\rangle \equiv (6s6n)\,^3S_1|F = 3/2, m_F = \pm 1/2\rangle$, where B is the magnetic field in units of Gauss.

According to the angular momentum selection rule, the Rabi frequencies $\Omega_{g\uparrow(\downarrow)}$ for the ground-Rydberg transition via the $(6s6p)\,^3P_1$ state, and the Rabi frequencies $\Omega_{cr\uparrow(\downarrow)}$ for the clock-Rydberg transition satisfy the condition [37]

$$\begin{aligned} &\Omega_{g\uparrow} = -\Omega_{g\downarrow}, \\ &\Omega_{c\uparrow} = \Omega_{c\downarrow}, \end{aligned} \tag{6}$$

where the ground-Rydberg transition is used in the creation of $|SB\rangle$ and $|\blacktriangle\rangle$. Note that Eq. (6) does not mean that the four entanglement protocols are limited to the forms shown. The nuclear-spin quantum gates in Sections 2.3 and 3 can also be executed by ground-Rydberg transitions for nuclear spins in the ground state, and other forms of $|SB\rangle$ and $|\blacktriangle\rangle$ can be prepared with the "g" and "c" states exchanged in the equations defining them.

For the nuclear-spin gates and the first two pulses of the entanglement protocols in Sections 4 and 5, the laser is tuned to the middle of the gap between the two Rydberg states $|r_+\rangle$ and $|r_-\rangle$ as shown in Fig. 1, i.e., the "detuning" of the Rydberg lasers are Δ and $-\Delta$ for $|r_+\rangle$ and $|r_-\rangle$, respectively, where the "detuning" is given by the transition frequency deducted by the laser frequency (which has a sign difference compared to the usual definition of detuning for the sake of convenience). The magnetic field is fixed, while the laser fields can be tuned so that Rydberg Rabi frequencies can be varied between pulses.

2.3 A three-pulse sequence

We consider a controlled-phase gate with three sequential laser pulses sent to the two atoms. The Hamiltonians for the gate are shown in Appendix A. According to Refs. [51, 52] and the Rydberg blockade condition [1], by applying a pulse of duration $\mathbb{T}_1 = 2\pi/\sqrt{\Delta^2 + 2\Omega_x^2}$, where

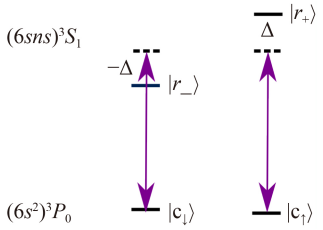

Fig. 1 Rydberg excitation of two nuclear-spin qubit states $|\uparrow\rangle$ and $|\downarrow\rangle$ in $|c_\uparrow\rangle \equiv |(6s^2)^3P_0|I = 1/2, m_I = 1/2\rangle$ and $|c_\downarrow\rangle \equiv |(6s^2)^3P_0|I = 1/2, m_I = -1/2\rangle$ to two respective Rydberg states $|r_-\rangle$ and $|r_+\rangle$, where c denotes the clock state with ^{171}Yb as an example. In a B-field of several Gauss (1 G= 10^{-4} T), the two nuclear spin states in the clock state are nearly degenerate compared to the MHz-scale Rabi frequencies considered in this paper. The laser fields are π polarized and tuned to the middle of the gap between $|r_+\rangle$ and $|r_-\rangle$.

$\Omega_{c\uparrow} = \Omega_{c\downarrow} \equiv \Omega_x$ [according to Eq. (6)] is the Rabi frequency in the x-th pulse, $x = 1, 2$, or 3, we have the state map

$$\begin{aligned} |c_\uparrow c_\uparrow\rangle &\to e^{-i\pi(1+\Delta/\sqrt{\Delta^2+2\Omega_x^2})}|c_\uparrow c_\uparrow\rangle, \\ |c_\downarrow c_\downarrow\rangle &\to e^{-i\pi(1-\Delta/\sqrt{\Delta^2+2\Omega_x^2})}|c_\downarrow c_\downarrow\rangle. \end{aligned}$$

For the first pulse, we find that when

$$\Omega_1/\Delta = 1.6088,$$

the states $|c_\uparrow c_\downarrow\rangle$ and $|c_\downarrow c_\uparrow\rangle$ are excited to states with unit Rydberg excitation. For example, driven by the Hamiltonian $(\Omega_{c\uparrow}|r_+\rangle\langle c_\uparrow| + \Omega_{c\downarrow}|r_-\rangle\langle c_\downarrow| + \text{H.c.})/2 + \Delta(|r_+\rangle\langle r_+| - |r_-\rangle\langle r_-|)$ for each atom, $|c_\uparrow c_\downarrow\rangle$ evolves to

$$(e^{i\varphi_+}|r_+ c_\downarrow\rangle + e^{i\varphi_-}|c_\uparrow r_-\rangle)/\sqrt{2}, \tag{7}$$

where $\varphi_+ = 2.645$ rad and $\varphi_- = 0.497$ rad. To map the state down to ground states, we find that it is necessary to change the phase of the Rydberg state, which is why we apply a second pulse in the condition

$$\Omega_2/\Delta = 0.5932e^{i3\pi/4}.$$

After the second pulse, the state in Eq. (7) becomes $e^{-i\varphi_+}|r_+ c_\downarrow\rangle + e^{-i\varphi_-}|c_\uparrow r_-\rangle)/\sqrt{2}$. Then, with a third pulse of condition

$$\Omega_3 = \Omega_1 e^{i\beta/2},$$

a gate in Eq. (4) is realized with $\alpha = 1.793$ rad in the ideal blockade condition. If $\beta = \pm\pi$ is chosen, a CZ gate is realized, for which a numerical simulation is shown in Fig. 2 with a finite V. The total duration of the gate is $\sum_{x=1}^{3}\mathbb{T}_x \approx \frac{5.054\pi}{\Omega_1}$, which is in terms of the maximal Rabi frequency Ω_1 (or Ω_3) during the three pulses. If we assume $|\Omega_1|/(2\pi) = 3.25$ MHz (corresponding to $\Delta/(2\pi) = 2.02$ MHz in a B-field of 2.1 G), the gate duration would be 0.78 μs. We use $|\Omega_x| \le 2\pi \times 3.25$ MHz in the numerical example for it is equal to the maximal Rabi

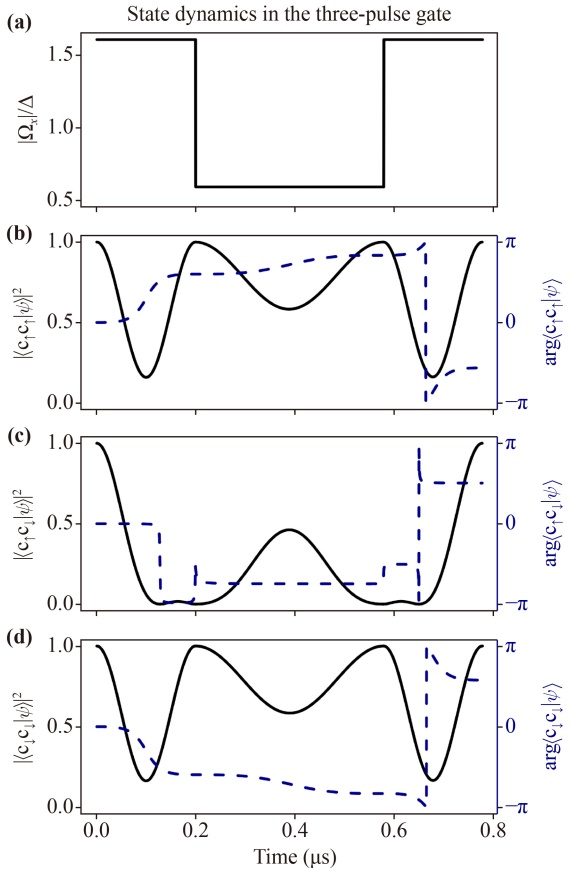

Fig. 2 State dynamics for different input states when ignoring Rydberg-state decay in the controlled-phase gate (with $\beta = -\pi$ as an example here). **(a)** $|\Omega_x|/\Delta$ as a function of time during the three pulses of the nuclear-spin gate. Here, the largest Rabi frequency is $|\Omega_1| = |\Omega_3| = 2\pi \times 3.25$ MHz, and the relative phases of the three Rabi frequencies are $0, 3\pi/4, -\pi/2$. The Rydberg interaction is $V_0/(2\pi) = 260$ MHz (its fluctuation is studied in Section 2.4). **(b–d)** show the population and phase of the ground-state component in the wavefunction when the input states for the gate protocol are $|c_\uparrow c_\uparrow\rangle$, $|c_\uparrow c_\downarrow\rangle$, and $|c_\downarrow c_\downarrow\rangle$, respectively. The final population errors in the target ground states are 2.6×10^{-5}, 2.1×10^{-5}, and 2.4×10^{-5} in (b), (c), and (d), respectively, and their final phases are -1.771, 1.587, and 1.816 rad, respectively. The state dynamics for the input state $|c_\downarrow c_\uparrow\rangle$ is similar to that of $|c_\uparrow c_\downarrow\rangle$.

frequencies used later on in creating $|SB\rangle$ and $|\blacktriangle\rangle$ in Sections 3 and 4, but in experiments much larger UV Rydberg Rabi frequencies are realizable since strong UV fields are available; for example, Rydberg Rabi frequencies up to $2\pi \times 13$ MHz were realized for exciting a Rydberg state of $n = 61$ with optimization of laser system and beam path [19].

2.4 Numerical analyses

Here, we numerically study the fidelity of the nuclear-spin gate. Because a CZ gate has the maximal entangling power among the two-qubit gates [53], we study the case with $\beta = -\pi$. Three main factors limit the intrinsic fidelity, the Rydberg state decay, the finiteness of V, and the fluctuation of V. The error due to Rydberg-state decay is [54]

$$E_{\text{decay}} = t_{\text{Ryd}}/\tau, \tag{8}$$

where t_{Ryd} is the Rydberg superposition time and τ is the lifetime of the Rydberg state. We numerically found $t_{\text{Ryd}} \approx \frac{2.7\pi}{\Omega_1}$. If the maximal Rabi frequency $|\Omega_1|$ is $2\pi \times 3.25$ MHz, the decay-induced error is $E_{\text{decay}} = 4.15 \times 10^{-3}$ with $\tau = 100$ μs estimated by using the lifetime of a lower state of $n = 59$ [23].

The analyses in Section 2.3 assumed infinite Rydberg interactions, but a blockade error will arise with finite V [52, 54]. The experiment of Ref. [20] estimated that the C_6 coefficient for the $|(6sns)^3S_1, F = I + 1\rangle$ state with $n = 50$ can be up to $2\pi \times 15$ GHz·μm^6. With the n^{11} scaling of van der Waals interaction, this would imply $C_6/(2\pi) = 15 \cdot (70/50)^{11} \approx 607$ GHz·μm^6 for the state we consider. To have a more conserved estimate about the gate fidelity in this paper, we use a smaller $C_6/(2\pi) = 192$ GHz·μm^6 from the analyses of Ref. [37]. We consider an atomic separation of 3 μm (this short atomic separation is possible since a value 2 μm was used in the experiment of Ref. [18]), for which we have $V_0/(2\pi) \approx 260$ MHz. The gate protocols in this paper do not need single-site addressing since all the pulses simultaneously excite all atoms. So, the small atomic separation does not bring extra difficulty. There is nearly no population loss to the states caused by the finiteness of V as shown in Fig. 2. With the finite V, the final phases for the four different input states differ from the desired ones. We numerically found that the protocol maps the states $\{|c_\uparrow c_\uparrow\rangle, |c_\uparrow c_\downarrow\rangle, |c_\downarrow c_\uparrow\rangle, |c_\downarrow c_\downarrow\rangle\}$ to $\{e^{-i\alpha'}|c_\uparrow c_\uparrow\rangle, e^{-i\beta'/2}|c_\uparrow c_\downarrow\rangle, e^{-i\beta'/2}|c_\downarrow c_\uparrow\rangle, e^{i\alpha''}|c_\downarrow c_\downarrow\rangle\}$ when the interaction is $V = V_0$, where $\{\alpha', \beta'/2, \alpha''\} \approx \{1.771, -1.587, 1.816\}$ rad. This means that by using $|c_\uparrow\rangle \rightarrowtail e^{i\alpha'/2}|c_\uparrow\rangle, |c_\downarrow\rangle \rightarrowtail e^{i(-\alpha'+\beta')/2}|c_\downarrow\rangle$, a gate of map $\text{diag}\{1, 1, 1, e^{i(\alpha''-\alpha'+\beta')}\}$ is realized, where $\alpha'' - \alpha' + \beta' \approx -3.128$ rad, which differs from $-\pi$ by about 0.0135 rad. To quantify the gate fidelity, we define

$$\hat{U} = \text{diag}\{e^{i(\theta-\alpha')}, e^{-i(\beta'/2+\theta)}, e^{-i(\beta'/2+\theta)}, e^{i(\alpha''+\theta)}\} \tag{9}$$

as the target gate map, where $\theta = -(\pi + \alpha'' - \alpha' + \beta')/4$. Then, using the single-qubit phase gates

$$|c_\uparrow\rangle \rightarrowtail e^{i(\alpha'-\theta)/2}|c_\uparrow\rangle,$$
$$|c_\downarrow\rangle \rightarrowtail e^{-i(\alpha'-\theta)/2+i(\beta'/2+\theta)}|c_\downarrow\rangle,$$

in both atoms one can transform Eq. (9) to the canonical CZ gate.

Beside that the finiteness of V can cause error, the fluctuation of V results in error, too. We define the rotation error by [55]

$$E_{\rm ro}=1-\frac{1}{20}\left[|{\rm Tr}(\hat{U}^{\dagger}\hat{\mathscr{U}})|^2+{\rm Tr}(\hat{U}^{\dagger}\hat{\mathscr{U}}\hat{\mathscr{U}}^{\dagger}\hat{U})\right], \tag{10}$$

where $\hat{\mathscr{U}}={\rm diag}\{{\rm e}^{{\rm i}\eta_1},{\rm e}^{{\rm i}\eta_2},{\rm e}^{{\rm i}\eta_3},{\rm e}^{{\rm i}\eta_4}\}$ is the state transform matrix with a fluctuating V, i.e., a V not equal to V_0. In order to evaluate the effect of fluctuation, we consider the average

$$\overline{E}_{\rm ro}=\frac{\int E_{\rm ro}(V){\rm d}V}{\int {\rm d}V}, \tag{11}$$

where the integration is over $V\in[(1-\epsilon)V_0,\ (1+\epsilon)V_0]$; we use a uniform distribution for it can lead to a larger gate error compared to a Gaussian distribution so that we can estimate the lower bound for the gate fidelity. The results shown in Fig. 3 indicate that the fluctuation of V does not result in small fidelities. Even when V tends to deviate from the desired interaction with $\epsilon=0.8$, we numerically found that the fidelity is $1-\overline{E}_{\rm ro}-E_{\rm decay}\approx 0.996$.

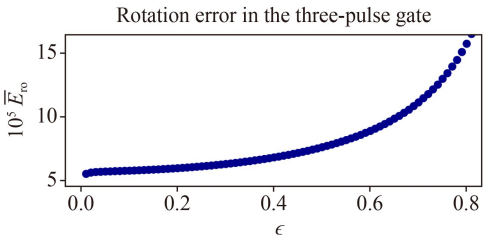

Fig. 3 Rotation error of the nuclear-spin gate (scaled by 10^5) of Eq. (10) averaged by uniformly varying the Rydberg interaction V in $[(1-\epsilon)V_0,\ (1+\epsilon)V_0]$, where $V_0/(2\pi)=260$ MHz. The fluctuation of V leads to phases different from the desired phases in Eq. (9). The largest Rabi frequency in the simulation is $|\Omega_1|/(2\pi)=3.25$ MHz shown in Fig. 2(a). The gate fidelity $1-\overline{E}_{\rm ro}-E_{\rm decay}$ is over 0.995 for the ϵ shown here, where the gate error is dominated by $E_{\rm decay}=4.15\times10^{-3}$ due to the short Rydberg state lifetime $\tau=100$ μs.

3 Faster gates assisted by Stark shifts

Here, we show that it is possible to realize the nuclear-spin gate in Section 2 with only two global pulses when assisted by Stark shifts. To be consistent with Section 2, we suppose that during the first pulse of the gate we use a rotating frame that transfers a Hamiltonian $\hat{\mathbb{H}}$ to ${\rm e}^{{\rm i}t\hat{R}}\hat{\mathbb{H}}{\rm e}^{-{\rm i}t\hat{R}}-\hat{R}\equiv\hat{H}$ with

$$\hat{R}=\omega(|r_+\rangle\langle r_+|+|r_-\rangle\langle r_-|),$$

where $\omega\pm\Delta=E_{\pm}$ is the energy separation (divided by the reduced Planck constant) between the clock state and $|r_{\pm}\rangle$, the energy is measured in reference to that of the clock state, and we ignore the energy separation between $|{\rm c}_{\uparrow}\rangle$ and $|{\rm c}_{\downarrow}\rangle$ since it is orders of magnitude smaller than the MHz-scale Rabi frequencies in a Gauss-scale magnetic field. In the second pulse, we assume that there are Stark shifts $\delta_{\pm}$ in $|r_{\pm}\rangle$ with the condition $\delta_-\delta_+=4\Delta$, and another rotating frame

$$\hat{R}'=(E_++\delta_++\Delta)|r_+\rangle\langle r_+|+(E_-+\delta_--\Delta)|r_-\rangle\langle r_-|$$

is used. In this new frame, the state in Eq. (7) becomes $({\rm e}^{{\rm i}\varphi'_+}|r_+{\rm c}_{\downarrow}\rangle+{\rm e}^{{\rm i}\varphi'_-}|{\rm c}_{\uparrow}r_-\rangle)/\sqrt{2}$, where $\varphi'_+=\varphi_++\mathbb{T}_1(\delta_++2\Delta)$ and $\varphi'_-=\varphi_-+\mathbb{T}_1(\delta_--2\Delta)$. With the condition $\delta_--\delta_+=4\Delta$, one can see that $\varphi'_+-\varphi_+=\varphi'_--\varphi_-$ which is equal to $\kappa=\mathbb{T}_1(\delta_++2\Delta)$. In other words, the frame transfer changes the state in Eq. (7) to

$${\rm e}^{{\rm i}\kappa}({\rm e}^{{\rm i}\varphi_+}|r_+{\rm c}_{\downarrow}\rangle+{\rm e}^{{\rm i}\varphi_-}|{\rm c}_{\uparrow}r_-\rangle)/\sqrt{2}, \tag{12}$$

while the four two-atom Rydberg states $|r_{\pm}r_{\pm}\rangle$ (which appear during the pulse sequence when V is finite) get an extra phase 2κ which is accounted for in the numerical simulation. By tuning the laser frequency to be at the middle between $|r_-\rangle$ and $|r_+\rangle$ and adding a phase $\pi+\beta/2+\kappa$ to the laser field, namely,

$$\Omega_2=-{\rm e}^{{\rm i}(\beta/2+\kappa)}\Omega_1,$$

the second pulse is with a Hamiltonian $[\Omega_2|r_+\rangle\langle{\rm c}_{\uparrow}|+\Omega_2|r_-\rangle\langle{\rm c}_{\downarrow}|+{\rm H.c.}]/2-\Delta(|r_+\rangle\langle r_+|-|r_-\rangle\langle r_-|)$ after dipole and rotating wave approximations. After the second pulse which has the same duration as the first one, we realize Eq. (4) with $\alpha=0$, and a CZ gate is realizable if $\beta=\pm\pi$ is chosen in the laser field. The total gate duration is $2\mathbb{T}_1\approx2.589\pi/\Omega_1$. A numerical simulation of the state dynamics for this two-pulse quantum gate is shown in Fig. 4 by assuming $\delta_-=4\Delta$ and $\delta_+=0$ (a different choice for the Stark shift does not bring difference to the target gate map).

We turn to the analyses of the gate fidelity with finite Rydberg interactions. With $V=V_0$, numerical simulation shows that the gate map is ${\rm diag}\{{\rm e}^{{\rm i}\nu},{\rm e}^{{\rm i}\mu},{\rm e}^{{\rm i}\mu},{\rm e}^{{\rm i}\nu}\}$, where $(\mu,\nu)\approx(-1.5583,0.02133)$ rad when $\beta=\pi$ and the state dynamics is shown in Fig. 4. The Rydberg superposition time is $t_{\rm Ryd}\approx1.47\pi/\Omega_1$ which leads to an error $E_{\rm decay}=2.26\times10^{-3}$ with $\Omega_1=2\pi\times3.25$ MHz and $\tau=100$ μs. To characterize the error from the finiteness and fluctuation of V, we define

$$\hat{\mathbb{U}}={\rm diag}\{{\rm e}^{{\rm i}(\nu+\vartheta)},{\rm e}^{{\rm i}(\mu-\vartheta)},{\rm e}^{{\rm i}(\mu-\vartheta)},{\rm e}^{{\rm i}(\nu+\vartheta)}\} \tag{13}$$

as the target gate, where $\vartheta=\pi/4-(\nu-\mu)/2\approx-0.004$ rad. By using the phase gates

$$|{\rm c}_{\uparrow}\rangle\rightarrowtail{\rm e}^{-{\rm i}(\nu+\vartheta)/2}|{\rm c}_{\uparrow}\rangle,$$
$$|{\rm c}_{\downarrow}\rangle\rightarrowtail{\rm e}^{{\rm i}(\nu-2\mu+3\vartheta)/2}|{\rm c}_{\downarrow}\rangle,$$

the map in Eq. (13) can be transformed to the CZ gate. We define the rotation error via Eq. (10) with $\hat{U}$ replaced by the matrix in Eq. (13), and evaluate the average infidelity as in Eq. (11), with the results shown in Fig. 5 which shows that with a large relative fluctuation

Table 1 Parameters for creating nuclear-spin controlled-phase gate of phase β. In the ideal blockade condition the gate map is diag$\{e^{-i\alpha}, e^{-i\beta/2}, e^{-i\beta/2}, e^{i\alpha}\}$, where α is about 1.79 rad in the three-pulse gate, and is zero in the two-pulse gate. A CZ gate is realized via single-qubit rotations when choosing $\beta = \pi$ for both cases here. κ is a phase to compensate an overall phase factor in the frame transform as discussed around Eq. (12).

		First pulse	Second pulse	Third pulse	Total duration
Three-pulse gate	Rabi frequency	1.6088Δ	$0.5932e^{i3\pi/4}\Delta$	$1.6088e^{i\beta/2}\Delta$	$3.14\pi/\Delta$
	pulse duration	$0.805\pi/\Delta$	$1.532\pi/\Delta$	$0.805\pi/\Delta$	or $5.05\pi/\Omega_m$
Two-pulse gate	Rabi frequency	1.6088Δ	$-1.6088e^{i(\beta/2+\kappa)}\Delta$	(not applicable)	$1.61\pi/\Delta$
	pulse duration	$0.805\pi/\Delta$	$0.805\pi/\Delta$		or $2.59\pi/\Omega_m$

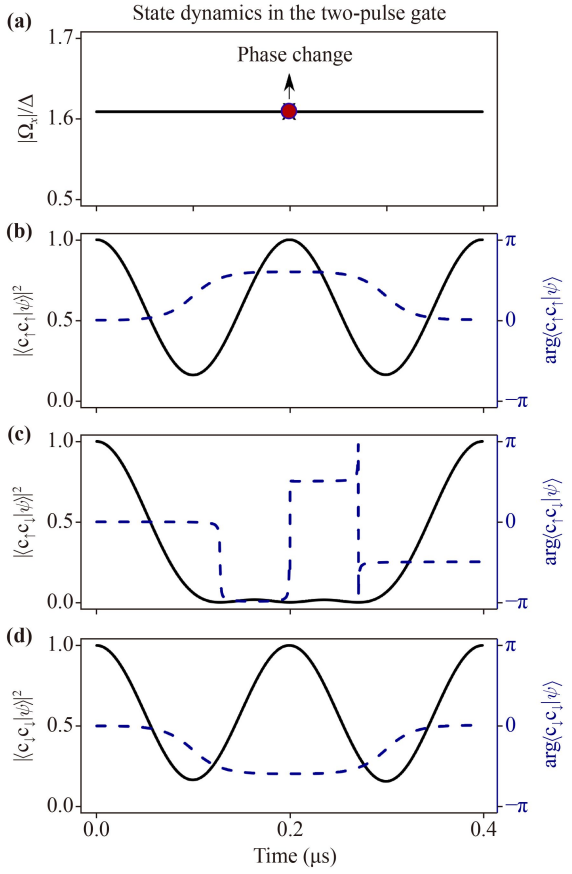

Fig. 4 State dynamics of the two-pulse nuclear-spin gate with $\beta = \pi$ and $|\Omega_2| = \Omega_1 \approx 2\pi \times 3.25$ MHz as an example. **(a)** The two laser pulses have the same strength and duration. The relative phase of the two Rabi frequencies are 0 and $\pi/2 + \kappa$, where κ is given above Eq. (12). A Stark shift $4\Delta \approx 8.08$ MHz was assumed in $|r_-\rangle$ during the second pulse, and the frequency of the laser during the second pulse increases by 2Δ compared to the first pulse. The Rydberg interaction is $V_0/(2\pi) = 260$ MHz. **(b–d)** show the population and phase of the ground-state component in the wavefunction when the input states for the gate protocol are $|c_\uparrow c_\uparrow\rangle$, $|c_\uparrow c_\downarrow\rangle$, and $|c_\downarrow c_\downarrow\rangle$, respectively. The final population errors in the target ground states are 4.4×10^{-5}, 1.24×10^{-4}, and 4.4×10^{-5} in (a), (b), and (c), respectively, and their final phases are 0.0213, −1.5583, and 0.0213 rad, respectively.

$\epsilon = 0.8$ of V, the gate still has a large fidelity 0.997 which is still limited by the Rydberg-state-decay error.

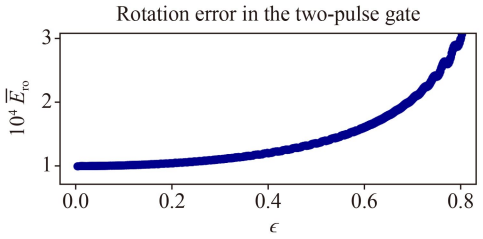

Fig. 5 Rotation error of the nuclear-spin gate (scaled by 10^4) averaged by uniformly varying the Rydberg interaction V in $[(1-\epsilon)V_0, (1+\epsilon)V_0]$, where $V_0/(2\pi) = 260$ MHz. Other parameters are the same as in Fig. 4. The gate fidelity $1 - \overline{E}_{ro} - E_{decay}$ is over 0.997 for the ϵ shown here, where the gate error is dominated by $E_{decay} = 2.26 \times 10^{-3}$.

4 Super Bell states

The SBS in Eq. (1) can be prepared starting from the following two-atom state

$$|\psi(0)\rangle = |cc\rangle_e \otimes (|\uparrow\uparrow\rangle_n + |\uparrow\downarrow\rangle_n + |\downarrow\uparrow\rangle_n + |\downarrow\downarrow\rangle_n)/2, \quad (14)$$

where the two-atom state is separable in that for each atom, the electronic state is in the optical clock state and the nuclear spin is in $(|\uparrow\rangle_n + |\downarrow\rangle_n)/\sqrt{2}$. Here, $\otimes$ is used because to a good approximation, the electron and nuclear spin are decoupled in the ground (g) and clock (c) states [35, 37, 45]. In Eq. (1), (θ, θ') are dependent on the Rydberg interactions and they approach $(0, \pi)$ in the ideal blockade condition. Because ${}_e\langle cc|\Phi\rangle_e = {}_n\langle\Psi|\Phi\rangle_n = 0$, one can define a pair of orthogonal two-atom electronic states

$$|+\rangle_e \equiv |cc\rangle_e,$$
$$|-\rangle_e \equiv |\Phi\rangle_n,$$

and a pair of orthogonal two-atom nuclear-spin states

$$|+\rangle_n \equiv |\Phi\rangle_n,$$
$$|-\rangle_n \equiv |\Psi\rangle_n,$$

so that Eq. (1) can also be written as

$$|SB\rangle \equiv \frac{1}{\sqrt{2}}\Big(|+\rangle_e \otimes |+\rangle_n + |-\rangle_e \otimes |-\rangle_n\Big), \quad (15)$$

which is a Bell state entangled between the electronic and nuclear spin states in two atoms. Combining Eqs. (2), (3), and (15), one can find that SBS is a "large" Bell state formed with three "smaller" Bell states and a product state $|cc\rangle_e$. As shown in Section 7, SBS can enable novel quantum dense coding [41].

4.1 A three-pulse protocol

We describe a three-pulse sequence for creating SBS.

4.1.1 The first pulse

First, with an ultra-violet (UV) laser excitation of pulse duration $\mathbb{T}_{p1}^{(S)}$,

$$\begin{aligned}|c_\uparrow\rangle &\xrightarrow[\text{detuned by}\Delta]{\Omega_{e\uparrow}=\Omega^{(s)}} |r_+\rangle,\\ |c_\downarrow\rangle &\xrightarrow[\text{detuned by}-\Delta]{\Omega_{e\downarrow}=\Omega^{(s)}} |r_-\rangle,\end{aligned}$$

the following state transform is realized,

$$\begin{aligned}&|c_\uparrow c_\uparrow\rangle \to e^{-i\hat{H}\mathbb{T}_{p1}^{(S)}}|c_\uparrow c_\uparrow\rangle,\\ &|c_\downarrow c_\downarrow\rangle \to e^{-i\hat{H}\mathbb{T}_{p1}^{(S)}}|c_\downarrow c_\downarrow\rangle,\\ &|c_\uparrow c_\downarrow\rangle \to |c_\uparrow c_\downarrow\rangle,\\ &|c_\downarrow c_\uparrow\rangle \to |c_\downarrow c_\uparrow\rangle,\end{aligned} \tag{16}$$

where $\hat{H}$ is the Hamiltonian shown in Appendix A. In the blockade regime, one can easily find, according to the picture of generalized Rabi oscillation [38, 51, 56, 57], that the last two transitions in Eq. (16) can be realized with a pulse duration $\mathbb{T}_{p1}^{(S)} = 2\pi/\sqrt{\Delta^2 + 0.5[\Omega^{(S)}]^2}$, where the ratio between Δ and Ω is determined in Sec. 4.1.2 below.

4.1.2 The second pulse

Second, with a two-photon Rydberg excitation of pulse duration $\mathbb{T}_{p2}^{(S)} = 2\pi/\sqrt{\Delta^2 + 0.5\eta^2[\Omega^{(S)}]^2}$,

$$\begin{aligned}|c_\uparrow\rangle &\xrightarrow[\text{detuned by}\Delta]{\Omega_{e\uparrow}=\eta\Omega^{(s)}} |r_+\rangle,\\ |c_\downarrow\rangle &\xrightarrow[\text{detuned by}-\Delta]{\Omega_{e\downarrow}=\eta\Omega^{(s)}} |r_-\rangle,\end{aligned}$$

the following state transform is realized,

$$\begin{aligned}&e^{-i\hat{H}\mathbb{T}_{p1}^{(S)}}|c_\uparrow c_\uparrow\rangle \to e^{i\alpha}\frac{|r_+c_\uparrow\rangle + |c_\uparrow r_+\rangle}{\sqrt{2}},\\ &e^{-i\hat{H}\mathbb{T}_{p1}^{(S)}}|c_\downarrow c_\downarrow\rangle \to e^{i(\pi-\alpha)}\frac{|r_-c_\downarrow\rangle + |c_\downarrow r_-\rangle}{\sqrt{2}},\\ &|c_\uparrow c_\downarrow\rangle \to |c_\uparrow c_\downarrow\rangle,\\ &|c_\downarrow c_\uparrow\rangle \to |c_\downarrow c_\uparrow\rangle,\end{aligned} \tag{17}$$

where the Hamiltonian is still in the form as in Appendix A. We find that with

$$\begin{aligned}&|\Omega^{(S)}|/\Delta = 1.608,\\ &\eta = -0.4606,\end{aligned} \tag{18}$$

the transitions in Eqs. (16) and (17) can be realized perfectly when V/Δ is infinite, where $\alpha = -0.8502$ (2.291) rad when $\Omega^{(S)}$ is positive (negative). Errors due to finite blockade will be analyzed later.

4.1.3 The third pulse

Before going to the third pulse, it is useful to point out that the description from Section 4.1.1 to Section 4.1.2 is in one rotating frame, and a different rotating frame is used in the third pulse. Details for this change of rotating frames is given in Appendix B, which shows that the frame transform changes the phase α in the first two equations of Eq. (17) to

$$\alpha' = \alpha + \Delta\left[\mathbb{T}_{p1}^{(S)} + \mathbb{T}_{p2}^{(S)}\right].$$

The third pulse is realized by two-photon Rydberg laser excitation of the transitions

$$\begin{aligned}|g_\uparrow\rangle &\xrightarrow{\Omega_{g\uparrow}=\Omega_{\text{eff}}(1+e^{2it\Delta})} |r_+\rangle,\\ |g_\downarrow\rangle &\xrightarrow{\Omega_{g\downarrow}=-\Omega_{\text{eff}}(1+e^{-2it\Delta})} |r_-\rangle,\end{aligned}$$

i.e., two sets of laser fields of equal strength are sent, one resonant with $|g_\uparrow\rangle \leftrightarrow |r_+\rangle$, the other resonant with $|g_\downarrow\rangle \leftrightarrow |r_-\rangle$, each with a Rabi frequency Ω_{eff} where eff denotes that it is derived by adiabatic elimination of the intermediate states [37]. According to Eq. (17), there is no Rydberg population in the states evolved from the input states $|c_\uparrow c_\downarrow\rangle$ and $|c_\downarrow c_\uparrow\rangle$, and only the states evolved from the two input states $|c_\uparrow c_\uparrow\rangle$ and $|c_\downarrow c_\downarrow\rangle$ respond to the third pulse. For the input state $|c_\uparrow c_\uparrow\rangle$ which is $e^{i\alpha'}\frac{|r_+c_\uparrow\rangle+|c_\uparrow r_+\rangle}{\sqrt{2}}$ at the beginning of the third pulse, the Hamiltonian is

$$\hat{H}_{\uparrow\uparrow} = \frac{\Omega_{g\uparrow}}{2}\frac{|r_+c_\uparrow\rangle + |c_\uparrow r_+\rangle}{\sqrt{2}}\frac{\langle g_\uparrow c_\uparrow| + \langle c_\uparrow g_\uparrow|}{\sqrt{2}} + \text{H.c.}$$

For the input state $|c_\downarrow c_\downarrow\rangle$ which is $e^{i(\pi-\alpha')}\frac{|r_-c_\downarrow\rangle+|c_\downarrow r_-\rangle}{\sqrt{2}}$, we have

$$\hat{H}_{\downarrow\downarrow} = \frac{\Omega_{g\downarrow}}{2}\frac{|r_-c_\downarrow\rangle + |c_\downarrow r_-\rangle}{\sqrt{2}}\frac{\langle g_\downarrow c_\downarrow| + \langle c_\downarrow g_\downarrow|}{\sqrt{2}} + \text{H.c.}$$

We have also shown the above Hamiltonians without using the collective entangled basis states in Appendix C. We find that with

$$|\Omega_{\text{eff}}|/\Delta = 0.7064, \tag{19}$$

the third pulse leads to the state transform

$$\mathrm{e}^{\mathrm{i}\alpha'}\frac{|r_+\mathrm{c}_\uparrow\rangle+|\mathrm{c}_\uparrow r_+\rangle}{\sqrt{2}}\to\mathrm{e}^{\mathrm{i}(\alpha'+\beta)}\frac{|\mathrm{g}_\uparrow\mathrm{c}_\uparrow\rangle+|\mathrm{c}_\uparrow\mathrm{g}_\uparrow\rangle}{\sqrt{2}},$$
$$\mathrm{e}^{\mathrm{i}(\pi-\alpha')}\frac{|r_-\mathrm{c}_\downarrow\rangle+|\mathrm{c}_\downarrow r_-\rangle}{\sqrt{2}}\to\mathrm{e}^{\mathrm{i}(\pi-\alpha'-\beta)}\frac{|\mathrm{g}_\downarrow\mathrm{c}_\downarrow\rangle+|\mathrm{c}_\downarrow\mathrm{g}_\downarrow\rangle}{\sqrt{2}},\tag{20}$$

with a pulse duration

$$\mathbb{T}_{\mathrm{p3}}^{(\mathrm{S})}=\frac{1.688\pi}{\Delta},$$

while the states $|\mathrm{c}_\uparrow\mathrm{c}_\downarrow\rangle$ and $|\mathrm{c}_\downarrow\mathrm{c}_\uparrow\rangle$ do not evolve. We have $\beta=-1.575$ rad when Ω_{eff} is positive, and $\beta=1.567$ when Ω_{eff} is negative.

By defining nuclear spin up and down states with

$$\begin{aligned}&\mathrm{new}|\uparrow\rangle_{\mathrm{n}}=\mathrm{e}^{\mathrm{i}(\alpha'+\beta)/2+\mathrm{i}\pi/4}|\uparrow\rangle_{\mathrm{n}},\\&\mathrm{new}|\downarrow\rangle_{\mathrm{n}}=\mathrm{e}^{-\mathrm{i}(\alpha'+\beta)/2+3\mathrm{i}\pi/4}|\downarrow\rangle_{\mathrm{n}},\\&\mathrm{new}|\mathrm{c}\rangle_{\mathrm{e}}=-\mathrm{i}|\mathrm{c}\rangle_{\mathrm{e}},\end{aligned}\tag{21}$$

the two final states in Eq. (20) are written as

$$\frac{|\mathrm{g}_\uparrow\mathrm{c}_\uparrow\rangle+|\mathrm{c}_\uparrow\mathrm{g}_\uparrow\rangle}{\sqrt{2}},\quad\frac{|\mathrm{g}_\downarrow\mathrm{c}_\downarrow\rangle+|\mathrm{c}_\downarrow\mathrm{g}_\downarrow\rangle}{\sqrt{2}}.$$

Looking through Eqs. (16), (17), (20), and the basis definition in Eq. (21), one can see that

$$\begin{aligned}&|\mathrm{c}_\uparrow\mathrm{c}_\uparrow\rangle\rightarrowtail\frac{|\mathrm{g}_\uparrow\mathrm{c}_\uparrow\rangle+|\mathrm{c}_\uparrow\mathrm{g}_\uparrow\rangle}{\sqrt{2}}=\frac{|\mathrm{cg}\rangle+|\mathrm{gc}\rangle}{\sqrt{2}}\otimes|\uparrow\uparrow\rangle,\\&|\mathrm{c}_\downarrow\mathrm{c}_\downarrow\rangle\rightarrowtail\frac{|\mathrm{g}_\downarrow\mathrm{c}_\downarrow\rangle+|\mathrm{c}_\downarrow\mathrm{g}_\downarrow\rangle}{\sqrt{2}}=\frac{|\mathrm{cg}\rangle+|\mathrm{gc}\rangle}{\sqrt{2}}\otimes|\downarrow\downarrow\rangle,\\&|\mathrm{c}_\uparrow\mathrm{c}_\downarrow\rangle\rightarrowtail|\mathrm{c}_\uparrow\mathrm{c}_\downarrow\rangle=|\mathrm{cc}\rangle_{\mathrm{e}}\otimes|\uparrow\downarrow\rangle,\\&|\mathrm{c}_\downarrow\mathrm{c}_\uparrow\rangle\rightarrowtail|\mathrm{c}_\downarrow\mathrm{c}_\uparrow\rangle=|\mathrm{cc}\rangle_{\mathrm{e}}\otimes|\downarrow\uparrow\rangle,\end{aligned}\tag{22}$$

is realized with a total duration $\sum_{x=1}^{3}\mathbb{T}_{\mathrm{px}}^{(\mathrm{S})}$ which is about $4.781\pi/\Delta$, or $7.687\pi/|\Omega^{(\mathrm{S})}|$, or $3.377\pi/|\Omega_{\mathrm{eff}}|$ with the relations shown in Eqs. (18) and (19). If we start from the state in Eq. (14), the transform in Eq. (22) leads to SBS in Eq. (1). A numerical simulation with a practical V is shown in Fig. 6.

4.1.4 Another SBS

Using a similar strategy as in Sections 4.1.1–4.1.3, one can find that starting from

$$|\psi(0)\rangle=|\mathrm{gg}\rangle_{\mathrm{e}}\otimes(|\uparrow\uparrow\rangle_{\mathrm{n}}+|\uparrow\downarrow\rangle_{\mathrm{n}}+|\downarrow\uparrow\rangle_{\mathrm{n}}+|\downarrow\downarrow\rangle_{\mathrm{n}})/2,$$

the following SBS

$$|SB\rangle'\equiv\frac{1}{\sqrt{2}}\left(|\mathrm{gg}\rangle_{\mathrm{e}}\otimes|\Phi\rangle_{\mathrm{n}}+|\Phi\rangle_{\mathrm{e}}\otimes|\Psi\rangle_{\mathrm{n}}\right)\tag{23}$$

can be prepared by following the three pulses in Sections 4.1.1, 4.1.2, and 4.1.3 with the UV laser excitation and the two-photon ground-Rydberg excitation exchanged.

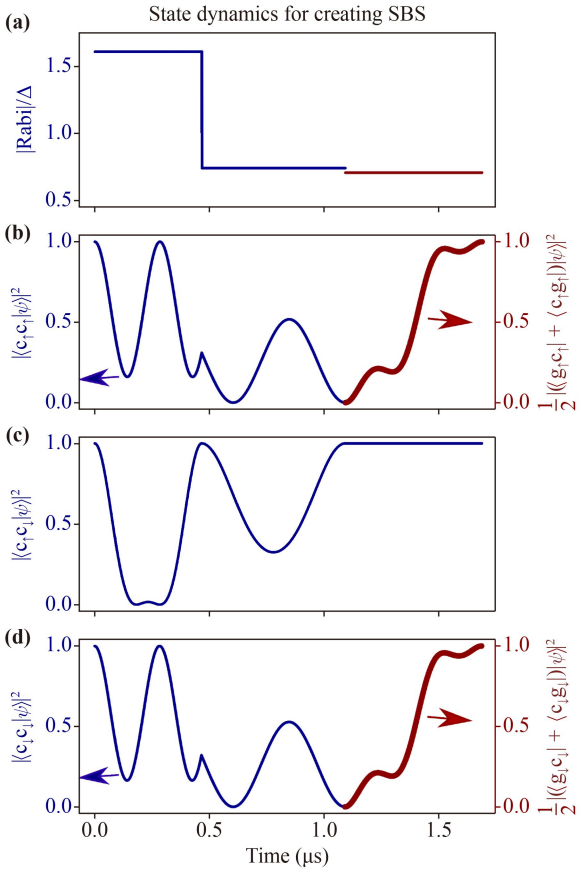

Fig. 6 State dynamics of the SBS protocol for different input states with $V_0/(2\pi)=260$ MHz and maximal Rabi frequency $\Omega^{(\mathrm{S})}/(2\pi)\approx 2.28$ MHz when ignoring Rydberg-state decay. **(a)** Magnitudes of Rabi frequencies in units of Δ. Here, the third pulse is with two-photon laser excitation, where one laser is resonant for the transition $|\mathrm{g}_\uparrow\rangle\to|r_+\rangle$ and the other laser resonant for $|\mathrm{g}_\downarrow\rangle\to|r_-\rangle$, each with a Rabi frequency $\Omega_{\mathrm{eff}}=2\pi\times 1$ MHz. These two lasers can be from one laser source via pulse pickers for shifting the frequency of one sub-beam by 2Δ. **(b–d)** show the population of the ground-state component in the wavefunction when the input states for the SBS protocol are $|\mathrm{c}_\uparrow\mathrm{c}_\uparrow\rangle$, $|\mathrm{c}_\uparrow\mathrm{c}_\downarrow\rangle$, and $|\mathrm{c}_\downarrow\mathrm{c}_\downarrow\rangle$, respectively. The thin (thick) curves in (b) and (d) denote population in the product (Bell) states. For the target ground states $|\Phi\rangle_{\mathrm{e}}\otimes|\uparrow\uparrow\rangle_{\mathrm{n}}$ in (b), $|\mathrm{c}_\uparrow\mathrm{c}_\downarrow\rangle$ in (c), and $|\Phi\rangle_{\mathrm{e}}\otimes|\downarrow\downarrow\rangle_{\mathrm{n}}$ in (d), the final populations are $1-1.4\times10^{-4}$, $1-3.1\times10^{-5}$, and $1-5.5\times10^{-5}$ respectively, and the final phases are $\Delta\left[\mathbb{T}_{\mathrm{p1}}^{(\mathrm{S})}+\mathbb{T}_{\mathrm{p2}}^{(\mathrm{S})}\right]-2.406$ rad, 0.009 rad, and $-\Delta\left[\mathbb{T}_{\mathrm{p1}}^{(\mathrm{S})}+\mathbb{T}_{\mathrm{p2}}^{(\mathrm{S})}\right]-0.697$ rad, respectively. These are different from those described in Sections 4.1.2 and 4.1.3 for the Rydberg interaction here is finite (its fluctuation is studied in Section 4.2).

The state in Eq. (23) can also be prepared from the SBS in Eq. (1) (with a trivial overall π phase). The method is simple, by using the ground-clock state transition

$$|\mathrm{g}\rangle_{\mathrm{e}}\leftrightarrow|\mathrm{c}\rangle_{\mathrm{e}}\tag{24}$$

with a duration π/Ω_{gc}, where Ω_{gc} is the Rabi frequency for the ground-clock transition, $|cc\rangle_e \to -|gg\rangle_e$ and $|\Phi\rangle_e \to -|\Phi\rangle_e$ are realized [56], leading to $|SB\rangle \to -|SB\rangle'$. As analyzed in Ref. [35], $\Omega_{gc} = 2\pi \times 0.2$ MHz can be realized, with which Eq. (23) can be formed from Eq. (1) with a pulse duration 2.5 μs.

4.2 Numerical analyses

Here, we numerically study the fidelity for creating SBS with the pulses of Sections 4.1.1, 4.1.2, and 4.1.3. Three main factors limit the fidelity, the Rydberg state decay, the finiteness of V, and the fluctuation of V.

The Rydberg state decay is inversely proportional to the Rabi frequencies in the protocol. The ground-Rydberg transition requires two-photon excitation, for which the Rabi frequency can be small. As analyzed in Ref. [37], $\Omega_{eff}/(2\pi) = 1.4$ MHz can be realized for exciting a Rydberg state with principal quantum number $n \sim 70$. During the third pulse of Section 4.1.3, two sets of two-photon transitions shall be used, one resonant with $|r_+\rangle$, and the other resonant with $|r_-\rangle$. To realize such transitions with one laser source for the ground-intermediate state transition, and another laser source for the intermediate-Rydberg state transition, the transition from the intermediate state to $|r_+\rangle$ and $|r_-\rangle$ can be realized by dividing the laser beam to two halves for which the frequency of one half shall be shifted by 2Δ via pulse pickers. This is experimentally feasible as shown in Ref. [39], where one laser source was used to drive a two-photon Raman transition assisted by several electro–optic modulators and crossed acousto–optic deflectors. This means that if we employ two lasers of similar powers in the analyses of Ref. [37], the available Ω_{eff} will be reduced by a factor of $\sqrt{2}$. For this reason, we assume $\Omega_{eff}/(2\pi) = 1$ MHz, which corresponds to $2\Delta/(2\pi) = 2.83$ MHz (realized with a B-field of 1.5 G) according to Eq. (19). By Eq (18), the UV laser Rabi frequencies are $\Omega^{(S)}/(2\pi) \approx 2.28$ MHz for the first pulse, and $|\eta|\Omega^{(S)}/(2\pi) \approx 1.05$ MHz for the second pulse. Concerning that the UV laser Rabi frequency can be quite large [35], the above analyses show that the speed for creating SBS is limited by the smaller two-photon ground-Rydberg Rabi frequency. Note, however, that the analyses in Ref. [37] were quite conservative, and in principle higher ground-Rydberg Rabi frequencies should be achievable. The error due to Rydberg-state decay is given by Eq. (8), where t_{Ryd} is the Rydberg superposition time. We numerically find $t_{Ryd} = 0.55\mathbb{T}_{p1} + 0.57\mathbb{T}_{p2} + 0.23\mathbb{T}_{p3}$. With $\Omega_{eff}/(2\pi) = 1$ MHz, and $\Omega^{(S)}$ and Δ given by Eqs. (18) and (19), we find $t_{Ryd} = 0.7506$ μs, leading to $E_{decay} = 7.51 \times 10^{-3}$ with $\tau = 100$ μs.

The analyses in Section 4.2 assumed infinite Rydberg interactions, but a finite V leads to population loss to the computational basis states. Moreover, it leads to some population of the two-atom Rydberg states $|r_+r_+\rangle, |r_+r_-\rangle, |r_-r_+\rangle$, and $|r_-r_-\rangle$ during the laser excitation, which alters the dynamics a little bit and finally leads to phases in the computational states different compared to those in Eq. (20). In other words, the final SBS with a certain V is no longer

$$\frac{1}{2}\Big[\frac{|cg\rangle + |gc\rangle}{\sqrt{2}} \otimes \left(e^{i(\alpha'+\beta)}|\uparrow\uparrow\rangle_n + e^{i(\pi-\alpha'-\beta)}|\downarrow\downarrow\rangle_n\right) + |cc\rangle_e \otimes (|\uparrow\downarrow\rangle_n + |\downarrow\uparrow\rangle_n)\Big],$$

but

$$\frac{1}{2}\Big[\frac{|cg\rangle + |gc\rangle}{\sqrt{2}} \otimes (\chi_1 e^{i\theta_1}|\uparrow\uparrow\rangle_n + \chi_2 e^{i\theta_2}|\downarrow\downarrow\rangle_n) + \chi_3 e^{i\theta_3}|cc\rangle_e \otimes (|\uparrow\downarrow\rangle_n + |\downarrow\uparrow\rangle_n)\Big],$$

where θ_1, θ_2, and θ_3 are dependent on V, and χ_1, χ_2, χ_3 should be 1 in the ideal case, but they are smaller than 1 due to the population loss when V is finite. To investigate the rotation error with finite V, we define

$$|SB_\theta\rangle = \frac{1}{2}\Big[\frac{|cg\rangle + |gc\rangle}{\sqrt{2}} \otimes \left(e^{i\theta_1}|\uparrow\uparrow\rangle_n + e^{i\theta_2}|\downarrow\downarrow\rangle_n\right) + e^{i\theta_3}|cc\rangle_e \otimes (|\uparrow\downarrow\rangle_n + |\downarrow\uparrow\rangle_n)\Big], \quad (25)$$

as the target SBS. Since a global phase is trivial, Eq. (25) can be written as Eq. (1) where $\theta = \theta_1 - \theta_3$ and $\theta' = \theta_2 - \theta_3$ in Eq. (2). The reason for the phase θ_1 of $\frac{|cg\rangle+|gc\rangle}{\sqrt{2}} \otimes |\uparrow\uparrow\rangle$ to differ from θ_2 of $\frac{|cg\rangle+|gc\rangle}{\sqrt{2}} \otimes |\downarrow\downarrow\rangle$ is that the detunings $V \pm 2\Delta$ for them are different, shown in Eqs. (A1) and (A2), which result in different state dynamics. With $V_0 = 2\pi \times 260$ MHz, we find

$$\theta_1 = -2.406 + \Delta(\mathbb{T}_{p1} + \mathbb{T}_{p2}),$$
$$\theta_2 = -0.697 - \Delta(\mathbb{T}_{p1} + \mathbb{T}_{p2}),$$
$$\theta_3 = 0.009.$$

By defining new nuclear-spin and clock states (or, using single-qubit phase gates),

$$\text{new}|\uparrow\rangle_n = e^{-i(2\theta_3 - 3\theta_1 - \theta_2)/4}|\uparrow\rangle_n,$$
$$\text{new}|\downarrow\rangle_n = e^{-i(2\theta_3 - \theta_1 - 3\theta_2)/4}|\downarrow\rangle_n,$$
$$\text{new}|c\rangle_e = e^{-i(\theta_1 + \theta_2 - 2\theta_3)/2}|c\rangle_e,$$

Eq. (25) can be formally written as

$$\frac{|cg\rangle_e + |gc\rangle_e}{2\sqrt{2}} \otimes (|\uparrow\uparrow\rangle_n + |\downarrow\downarrow\rangle_n) + \frac{|cc\rangle_e}{2} \otimes (|\uparrow\downarrow\rangle_n + |\downarrow\uparrow\rangle_n).$$

However, the target state is still Eq. (25), in which the angles θ_k, $k = 1, 2, 3$ fluctuate when V fluctuates due to the position fluctuation of the two atoms, leading to a rotation error,

$$E_{ro} = 1 - \langle SB_\theta|\hat{\rho}|SB_\theta\rangle, \quad (26)$$

where $\hat{\rho}$ is the density matrix of the actual state realized with the three-pulse protocol. Because the Rydberg-state

decay is analytically approximated above so as to get an upper bound for the error [54], we use unitary dynamics to simulate the blockade error so that Eq. (26) reduces to $1-|\langle\psi|SB\rangle|^2$ where $|\psi\rangle$ is the final state evolved from Eq. (14). To evaluate the rotation error, we consider the average $\overline{E}_{\rm ro}=\int E_{\rm ro}(V)\mathrm{d}V/\int \mathrm{d}V$, where the integration is over $V\in[(1-\epsilon)V_0,\ (1+\epsilon)V_0]$. To have a lower bound for the fidelity, we consider a uniform distribution of V instead of a Gaussian distribution. The numerical results for different ϵ are shown in Fig. 7. We find that for $\epsilon<0.55$, the average rotation error $\overline{E}_{\rm ro}$ is smaller than 10^{-4}. Remarkably, even with $\epsilon=0.8$, $\overline{E}_{\rm ro}$ is 2.14×10^{-4}. Different from entanglement protocols that require matching the Rydberg interaction with laser detuning [58, 59], the robustness here benefits from the intrinsic property of the blockade mechanism [47]. The fidelity $\mathcal{F}=1-\overline{E}_{\rm ro}-E_{\rm decay}$ for creating SBS is about 99.2% for ϵ up to 0.8, which is dominated by the Rydberg-state decay. This fidelity should be possible to be improved if larger ground-Rydberg Rabi frequencies are available.

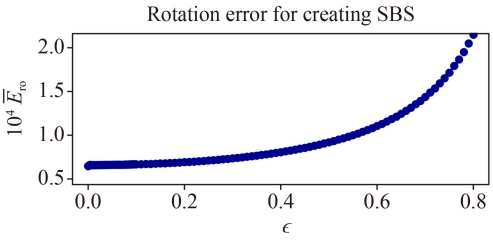

Fig. 7 Rotation error (scaled by 10^4) of Eq. (26) averaged by uniformly varying the Rydberg interaction V in $[(1-\epsilon)V_0,\ (1+\epsilon)V_0]$ for creating SBS. Here, $V_0/(2\pi)=260$ MHz, $\Omega_{\rm eff}/(2\pi)=1$ MHz, and $\Omega^{(\rm S)}$ and Δ are given by Eqs. (18) and (19). The fidelity of SBS generation, $1-\overline{E}_{\rm ro}-E_{\rm decay}$, is about 0.992 dominated by the Rydberg-state decay $E_{\rm decay}=7.51\times10^{-3}$ due to the short Rydberg state lifetime $\tau=100\ \mu$s.

5 A three-atom state including W and GHZ states

5.1 A three-pulse protocol

Here, we show a three-pulse protocol to excite the initial product state

$$\begin{aligned}|\psi(0)\rangle =&|\mathrm{ccc}\rangle_{\rm e}\otimes(|\uparrow\uparrow\uparrow\rangle_{\rm n}+|\uparrow\uparrow\downarrow\rangle_{\rm n}+|\uparrow\downarrow\uparrow\rangle_{\rm n}\\&+|\downarrow\uparrow\uparrow\rangle_{\rm n}+|\uparrow\downarrow\downarrow\rangle_{\rm n}+|\downarrow\uparrow\downarrow\rangle_{\rm n}+|\downarrow\downarrow\uparrow\rangle_{\rm n}\\&+|\downarrow\downarrow\downarrow\rangle_{\rm n})/(2\sqrt{2})\end{aligned}\tag{27}$$

to realize $|\blacktriangle\rangle$ in Eq. (3). We will do it briefly for the pulses induce state transform similar to that in Section 4.1.

In the first pulse, a UV laser with a pulse duration $\mathbb{T}_{\rm p1}^{(\blacktriangle)}$ for the transitions

$$\begin{aligned}&|\mathrm{c}_\uparrow\rangle\xrightarrow[\text{detuned by }\Delta]{\Omega_{\mathrm{c}\uparrow}=\Omega^{(\blacktriangle)}}|r_+\rangle,\\&|\mathrm{c}_\downarrow\rangle\xrightarrow[\text{detuned by }-\Delta]{\Omega_{\mathrm{c}\downarrow}=\Omega^{(\blacktriangle)}}|r_-\rangle\end{aligned}$$

evolves the the input states as $|\mathrm{c}_x\mathrm{c}_y\mathrm{c}_z\rangle\to\mathrm{e}^{-\mathrm{i}\hat{H}\mathbb{T}_{\rm p1}^{(\blacktriangle)}}|\mathrm{c}_x\mathrm{c}_y\mathrm{c}_z\rangle$ where $x,y,z\in\{\uparrow,\downarrow\}$. Unlike the case for creating SBS, each input state here is in superposition of the clock and Rydberg states after the first pulse. The second pulse for the excitation

$$\begin{aligned}&|\mathrm{c}_\uparrow\rangle\xrightarrow[\text{detuned by }\Delta]{\Omega_{\mathrm{c}\uparrow}=\eta^{(\blacktriangle)}\Omega^{(\blacktriangle)}}|r_+\rangle,\\&|\mathrm{c}_\downarrow\rangle\xrightarrow[\text{detuned by }-\Delta]{\Omega_{\mathrm{c}\downarrow}=\eta^{(\blacktriangle)}\Omega^{(\blacktriangle)}}|r_-\rangle,\end{aligned}$$

of duration $\mathbb{T}_{\rm p2}^{(\blacktriangle)}$ leads to

$$\begin{aligned}&\mathrm{e}^{-\mathrm{i}\hat{H}\mathbb{T}_{\rm p1}^{(\blacktriangle)}}|\mathrm{c}_\uparrow\mathrm{c}_\uparrow\mathrm{c}_\uparrow\rangle\to\frac{\mathrm{e}^{\mathrm{i}\alpha^{(\blacktriangle)}}}{\sqrt{3}}(|r_+\mathrm{c}_\uparrow\mathrm{c}_\uparrow\rangle+|\mathrm{c}_\uparrow r_+\mathrm{c}_\uparrow\rangle\\&\qquad+|\mathrm{c}_\uparrow\mathrm{c}_\uparrow r_+\rangle),\\&\mathrm{e}^{-\mathrm{i}\hat{H}\mathbb{T}_{\rm p1}^{(\blacktriangle)}}|\mathrm{c}_\downarrow\mathrm{c}_\downarrow\mathrm{c}_\downarrow\rangle\to\frac{\mathrm{e}^{\mathrm{i}(\pi-\alpha^{(\blacktriangle)})}}{\sqrt{3}}(|r_-\mathrm{c}_\downarrow\mathrm{c}_\downarrow\rangle+|\mathrm{c}_\downarrow r_-\mathrm{c}_\downarrow\rangle\\&\qquad+|\mathrm{c}_\downarrow\mathrm{c}_\downarrow r_-\rangle),\end{aligned}\tag{28}$$

and

$$\mathrm{e}^{-\mathrm{i}\hat{H}\mathbb{T}_{\rm p1}^{(\blacktriangle)}}|\mathrm{c}_x\mathrm{c}_y\mathrm{c}_z\rangle\to\mathrm{e}^{\mathrm{i}\zeta^{(\blacktriangle)}}|\mathrm{c}_x\mathrm{c}_y\mathrm{c}_z\rangle,\tag{29}$$

when one of x,y, and z is $\downarrow$ while the other two are $\uparrow$, and

$$\mathrm{e}^{-\mathrm{i}\hat{H}\mathbb{T}_{\rm p1}^{(\blacktriangle)}}|\mathrm{c}_x\mathrm{c}_y\mathrm{c}_z\rangle\to\mathrm{e}^{-\mathrm{i}\zeta^{(\blacktriangle)}}|\mathrm{c}_x\mathrm{c}_y\mathrm{c}_z\rangle,\tag{30}$$

when one of x,y, and z is $\uparrow$ while the other two are $\downarrow$. We find that when

$$\begin{aligned}&|\Omega^{(\blacktriangle)}|=1.976\Delta,\\&\eta^{(\blacktriangle)}=-0.3735,\\&\mathbb{T}_{\rm p1}^{(\blacktriangle)}=5.933\pi/|\Omega^{(\blacktriangle)}|,\\&\mathbb{T}_{\rm p2}^{(\blacktriangle)}=1.902\pi/|\Omega^{(\blacktriangle)}|,\end{aligned}\tag{31}$$

the transitions in Eqs. (28), (29) and (30) can be realized with a fidelity over 0.995 for each input state. For infinite V/Δ, $\alpha^{(\blacktriangle)}$ is -1.036 (2.106) rad when $\Omega^{(\blacktriangle)}$ is positive (negative), and $\zeta^{(\blacktriangle)}=-0.8717$ rad. After the frame transform as in Appendix B, the angle $\alpha^{(\blacktriangle)}$ in the state on the right side of Eq. (28) becomes

$$\alpha^{(\blacktriangle)\prime}=\alpha^{(\blacktriangle)}+\Delta(\mathbb{T}_{\rm p1}^{(\blacktriangle)}+\mathbb{T}_{\rm p2}^{(\blacktriangle)}),$$

while $\zeta^{(\blacktriangle)}$ in Eqs. (29) and (30) remains the same. The third pulse induces a ground-Rydberg transition as in Section 4.1.3. We find that with the condition

$$\begin{aligned}&|\Omega_{\rm eff}^{(\blacktriangle)}|=0.6072\Delta,\\&\mathbb{T}_{\rm p3}^{(\blacktriangle)}=1.789\pi/\Delta,\end{aligned}\tag{32}$$

Table 2 Parameters for creating the two-atom super Bell state of Eq. (1) and the three-atom entangled state of Eq. (3).

	Initial state	Final state	First pulse (clock-Rydberg)	Second pulse (clock-Rydberg)	Third pulse (ground-Rydberg)	Total duration
$\|SB\rangle$	$\prod \frac{\|c_\uparrow\rangle+\|c_\downarrow\rangle}{\sqrt{2}}$	$\frac{1}{\sqrt{2}}(\|cc\rangle_e \otimes \|\Phi\rangle_n$ $+\|\Phi\rangle_e \otimes \|\Psi\rangle_n)$	Rabi: $\Omega^{(S)} = 1.608\Delta$ $\mathbb{T}_{p1} : 2.12\pi/\Omega^{(S)}$	Rabi: $-0.4606\Omega^{(S)}$ $\mathbb{T}_{p2} : 2.85\pi/\Omega^{(S)}$	Rabi: $0.4393\Omega^{(S)}$ $\mathbb{T}_{p3} : 2.71\pi/\Omega^{(S)}$	$7.69\pi/\Omega^{(S)}$
$\|\blacktriangle\rangle$	$\prod \frac{\|c_\uparrow\rangle+\|c_\downarrow\rangle}{\sqrt{2}}$	$\frac{1}{2}[(\sqrt{3}\|ccc\rangle_e \otimes \|\not{\#}\rangle_n$ $+\|W\rangle_e \otimes \|GHZ\rangle_n)]$	Rabi: $\Omega^{(\blacktriangle)} = 1.976\Delta$ $\mathbb{T}_{p1}^{(\blacktriangle)}$: $5.93\pi/\Omega^{(\blacktriangle)}$	Rabi: $-0.3735\Omega^{(\blacktriangle)}$ $\mathbb{T}_{p2}^{(\blacktriangle)} : 1.9\pi/\Omega^{(\blacktriangle)}$	Rabi: $0.3073\Omega^{(\blacktriangle)}$ $\mathbb{T}_{p3}^{(\blacktriangle)}$: $3.54\pi/\Omega^{(\blacktriangle)}$	$11.4\pi/\Omega^{(\blacktriangle)}$

the third pulse can restore the population in the states of Eq. (28) back to the ground states, i.e., the states in Eq. (28) evolve as

$$\begin{aligned}
&\frac{e^{i\alpha^{(\blacktriangle)\prime}}}{\sqrt{3}}(|r_+c_\uparrow c_\uparrow\rangle + |c_\uparrow r_+ c_\uparrow\rangle + |c_\uparrow c_\uparrow r_+\rangle)\\
&\to \frac{e^{i[\alpha^{(\blacktriangle)\prime}+\beta^{(\blacktriangle)}]}}{\sqrt{3}}(|g_\uparrow c_\uparrow c_\uparrow\rangle + |c_\uparrow g_\uparrow c_\uparrow\rangle + |c_\uparrow c_\uparrow g_\uparrow\rangle)\\
&= e^{i[\alpha^{(\blacktriangle)\prime}+\beta^{(\blacktriangle)}]}|W\rangle_e \otimes |\uparrow\uparrow\uparrow\rangle_n,\\
&\quad - \frac{e^{-i\alpha^{(\blacktriangle)\prime}}}{\sqrt{3}}(|r_-c_\downarrow c_\downarrow\rangle + |c_\downarrow r_- c_\downarrow\rangle + |c_\downarrow c_\downarrow r_-\rangle)\\
&\to -\frac{e^{i[-\alpha^{(\blacktriangle)\prime}-\beta^{(\blacktriangle)}]}}{\sqrt{3}}(|g_\downarrow c_\downarrow c_\downarrow\rangle + |c_\downarrow g_\downarrow c_\downarrow\rangle + |c_\downarrow c_\downarrow g_\downarrow\rangle)\\
&= -e^{i[-\alpha^{(\blacktriangle)\prime}-\beta^{(\blacktriangle)}]}|W\rangle_e \otimes |\downarrow\downarrow\downarrow\rangle_n,
\end{aligned}$$

where $\beta^{(\blacktriangle)} = -1.607$ (1.534) rad when $\Omega_{\rm eff}^{(\blacktriangle)}$ is positive (negative), while the states in Eqs. (29) and (30) remain the same because the third pulse excites the ground-Rydberg transitions. So, starting from the state of Eq. (27), the above pulses realize the state

$$\begin{aligned}
&\frac{1}{2}\Big\{\frac{\sqrt{6}}{2}|ccc\rangle_e \otimes \Big[e^{i\zeta^{(\blacktriangle)}}\frac{|\uparrow\uparrow\downarrow\rangle_n + |\uparrow\downarrow\uparrow\rangle_n + |\downarrow\uparrow\uparrow\rangle_n}{\sqrt{3}}\\
&\quad + e^{-i\zeta^{(\blacktriangle)}}\frac{|\uparrow\downarrow\downarrow\rangle_n + |\downarrow\uparrow\downarrow\rangle_n + |\downarrow\downarrow\uparrow\rangle_n}{\sqrt{3}}\Big]\\
&\quad + |W\rangle_e \otimes \frac{e^{i[\alpha^{(\blacktriangle)\prime}+\beta]}|\uparrow\uparrow\uparrow\rangle_n - e^{-i[\alpha^{(\blacktriangle)\prime}+\beta]}|\downarrow\downarrow\downarrow\rangle_n}{\sqrt{2}})\Big\},
\end{aligned}$$

in which the relative phase in the nuclear-spin GHZ state can be removed by redefining the basis states. The total duration is about $11.43\pi/|\Omega^{(\blacktriangle)}|$ for creating $|\blacktriangle\rangle$. A numerical test of the above protocol is shown in Fig. 8 with relevant Hamiltonians shown in Appendix D.

5.2 Numerical simulations

We consider three atoms forming a triangle in the x–y plane when the laser fields are sent along z [12, 17], and the atoms are in a configuration where the three distances between atom traps are equal as in the experiment [18]. To have equal laser-field strength for the three atoms, the laser is focused at the center of the triangle. When there is no fluctuation of the atomic positions, the interactions between any two Rydberg atoms are equal to the desired value V_0. Even so, the final state has some population loss in the target state mainly due to the finiteness of V, as shown in Fig. 8.

The Rydberg-state decay induces an error $E_{\rm decay} \approx 2.51\pi/(\tau\Delta)$, which is about 7.62×10^{-3} when $\Omega_{\rm eff}^{(\blacktriangle)}/(2\pi) = 1$ MHz and $\tau = 100$ μs. The fluctuation of V and its finiteness result in gate errors analyzed as follows. We define the state with state phases realized when $V = V_0$ as the target state

$$\begin{aligned}
|\blacktriangle_\theta\rangle =&\frac{1}{2}\Big\{\frac{\sqrt{6}}{2}|ccc\rangle_e \otimes \Big[e^{i\vartheta_1}\frac{|\uparrow\uparrow\downarrow\rangle_n + |\uparrow\downarrow\uparrow\rangle_n + |\downarrow\uparrow\uparrow\rangle_n}{\sqrt{3}}\\
&+ e^{i\vartheta_2}\frac{|\uparrow\downarrow\downarrow\rangle_n + |\downarrow\uparrow\downarrow\rangle_n + |\downarrow\downarrow\uparrow\rangle_n}{\sqrt{3}}\Big]\\
&+ |W\rangle_e \otimes \frac{e^{i\vartheta_3}|\uparrow\uparrow\uparrow\rangle_n + e^{i\vartheta_4}|\downarrow\downarrow\downarrow\rangle_n}{\sqrt{2}}\Big\},
\end{aligned} \tag{33}$$

where the four angles $\vartheta_k, k = 1$–4 are given in the caption of Fig. 8. If we define new nuclear-spin states by absorbing phases to them as

$$\begin{aligned}
{\rm new}|g\rangle_e &= e^{i(2\vartheta_4+7\vartheta_3-6\vartheta_1)/9}|g\rangle_e,\\
{\rm new}|c\rangle_e &= e^{i(3\vartheta_1+\vartheta_3-\vartheta_4)/9}|c\rangle_e,\\
{\rm new}|\downarrow\rangle_n &= e^{i(\vartheta_4-\vartheta_3)/3}|\downarrow\rangle_n,
\end{aligned} \tag{34}$$

the four phases ϑ_1–ϑ_4 of the state in Eq. (33) become $0, \vartheta_2-\vartheta_1+(\vartheta_3-\vartheta_4)/3$, 0, and 0, respectively. The basis transform is not necessary since in real experiments the interesting part of the state is the electrons–nuclei entanglement. So, the state in Eq. (33) is the target $|\blacktriangle\rangle$ state. To quantify the error from the fluctuation of V, we define $E_{\rm ro} = 1 - \langle\blacktriangle_\theta|\hat{\rho}|\blacktriangle_\theta\rangle$ as the rotation error, where $\hat{\rho}$ is the density matrix of the actual state realized with the three-pulse protocol. With unitary dynamics, the rotation error becomes $1 - |\langle\psi|\blacktriangle_\theta\rangle|^2$ where $|\psi\rangle$ is the final state evolved from Eq. (14). To evaluate the rotation error, we consider the average $\overline{E}_{\rm ro} = \int E_{\rm ro}(V){\rm d}V/\int {\rm d}V$, where the integration is over $V \in [(1-\epsilon)V_0, (1+\epsilon)V_0]$. With a uniform distribution of V, the numerical results for different ϵ are shown in Fig. 9. The average rotation error $\overline{E}_{\rm ro}$ increases from 2 to 4.5×10^{-3} when ϵ grows from 0 to 0.8. The fidelity can be about 0.988 if ϵ is as large as 0.8.

Note that the numerical example shown above can be

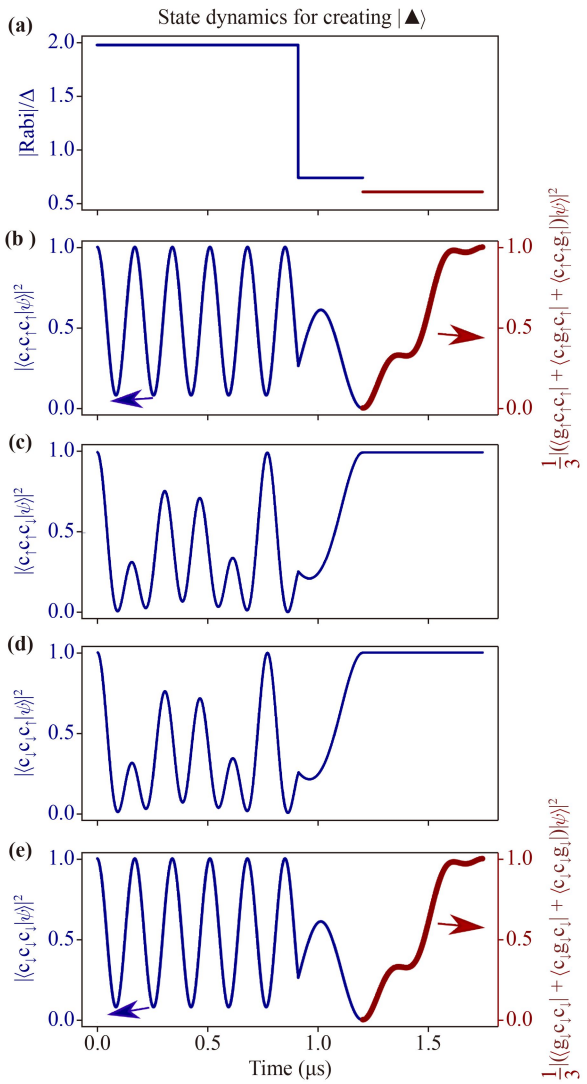

Fig. 8 State dynamics of the $|\blacktriangle\rangle$ protocol for different input states with $V_0/(2\pi) = 260$ MHz and maximal Rabi frequency $\Omega^{(\blacktriangle)}/(2\pi) \approx 3.25$ MHz when ignoring Rydberg-state decay. **(a)** Magnitudes of Rabi frequencies in units of Δ. **(b–e)** show the population of the ground-state component in the wavefunction when the input states for the gate protocol are $|c_\uparrow c_\uparrow c_\uparrow\rangle$, $|c_\uparrow c_\uparrow c_\downarrow\rangle$, $|c_\downarrow c_\downarrow c_\uparrow\rangle$, and $|c_\downarrow c_\downarrow c_\downarrow\rangle$, respectively. The thin and thick curves in (b) and (e) denote population in the product and W states, respectively. For the target ground states $|W\rangle_e \otimes |\uparrow\uparrow\uparrow\rangle_n$ in (b), $|c_\uparrow c_\uparrow c_\downarrow\rangle$ in (c), $|c_\downarrow c_\downarrow c_\uparrow\rangle$ in (d), and $|W\rangle_e \otimes |\downarrow\downarrow\downarrow\rangle_n$ in (e), the final populations are 0.9986, 0.9968, 0.9988, and 0.9982 respectively, and the final phases are $\vartheta_1 = \Delta\left[\mathbb{T}_{p1}^{(\blacktriangle)} + \mathbb{T}_{p2}^{(\blacktriangle)}\right] - 2.532$ rad, $\vartheta_2 = -0.7648$ rad, $\vartheta_3 = 0.9795$ rad, and $\vartheta_4 = -\Delta\left[\mathbb{T}_{p1}^{(\blacktriangle)} + \mathbb{T}_{p2}^{(\blacktriangle)}\right] - 0.385$ rad, respectively.

optimized so as to have a faster preparation of the state. For example, Appendix E shows another set of parameters to create $|\blacktriangle\rangle$ with a faster speed. The purpose of this paper is to reveal the possibility to create exotic multi-atom entanglement between electrons and nuclear spins.

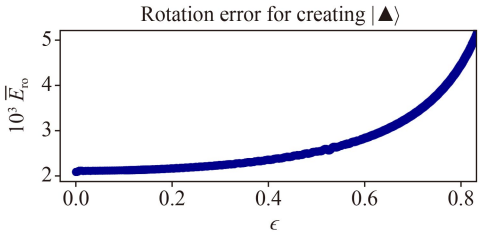

Fig. 9 Rotation error (scaled by 10^3) averaged by uniformly varying the Rydberg interaction V in $[(1-\epsilon)V_0, (1+\epsilon)V_0]$ for creating $|\blacktriangle\rangle$. Here, $V_0/(2\pi) = 260$ MHz, $\Omega_{\rm eff}^{(\blacktriangle)}/(2\pi) = 1$ MHz, and $\Omega^{(\blacktriangle)}$ and Δ are given by Eqs. (31) and (32). The fidelity to generate $|\blacktriangle\rangle$ in the form of Eq. (33), $1 - \overline{E}_{ro} - E_{decay}$, is about 0.988 for $\epsilon = 0.8$.

6 Realizing lower-dimensional entanglement by measurement

SBS and $|\blacktriangle\rangle$ are highly entangled. Here, we show how to use them to create other types of entangled states. Taking SBS as an example, SBS incorporates three small Bell states as discussed in Section 3 and it is a Bell-like state by itself, shown in Eq. (15). This means that it is in principle possible to extract the "smaller" Bell states from it.

6.1 Measurement of one atom at a time in SBS

Below, we show that by measuring one or two atoms, the SBS in Eq. (25) can be projected to different entangled states depending on the measurement results. In other words, it is possible to create lower-dimensional entanglement by measurement of SBS.

By measuring one of the two atoms, one can determine whether the atom is in the ground state or not by detecting the light scattered via the transition between the ground state and $(6s6p)^1P_1$) [40]. However, we need to ensure that the measurement does not change the nuclear-spin states which demands efforts to quench the hyperfine-interaction-induced spin mixing [32, 33]. If the first atom is measured, and the result is that no light is detected, the state in Eq. (25) becomes

$$|\xi_1\rangle = \frac{1}{\sqrt{6}}\Big[|cg\rangle_e \otimes \left(e^{i\theta_1}|\uparrow\uparrow\rangle_n + e^{i\theta_2}|\downarrow\downarrow\rangle_n\right) + e^{i\theta_3}\sqrt{2}|cc\rangle_e \otimes (|\uparrow\downarrow\rangle_n + |\downarrow\uparrow\rangle_n)\Big]. \quad (35)$$

Then, measuring the second atom in the state of Eq. (35) has two outcomes. If no light is detected, the state in Eq. (35) collapses to

$$|\xi_{1a}\rangle = \frac{1}{\sqrt{2}}|cc\rangle_e \otimes (|\uparrow\downarrow\rangle_n + |\downarrow\uparrow\rangle_n), \quad (36)$$

but if light is detected, the state in Eq. (35) collapses to

$$|\xi_{1b}\rangle = \frac{1}{\sqrt{2}}|\mathrm{cg}\rangle_\mathrm{e} \otimes \left(\mathrm{e}^{\mathrm{i}\theta_1}|\uparrow\uparrow\rangle_\mathrm{n} + \mathrm{e}^{\mathrm{i}\theta_2}|\downarrow\downarrow\rangle_\mathrm{n}\right). \quad (37)$$

When the measurement of the first atom results in light detected, meaning that the atom is in $|\mathrm{g}\rangle$, the state in Eq. (25) becomes

$$|\xi_2\rangle = \frac{1}{\sqrt{2}}|\mathrm{gc}\rangle_\mathrm{e} \otimes \left(\mathrm{e}^{\mathrm{i}\theta_1}|\uparrow\uparrow\rangle_\mathrm{n} + \mathrm{e}^{\mathrm{i}\theta_2}|\downarrow\downarrow\rangle_\mathrm{n}\right). \quad (38)$$

The state in Eq. (36) is an entangled nuclear-spin state in the clock state. The states in Eqs. (37) and (38) can be converted to

$$|\xi'_{1b}\rangle = |\mathrm{gg}\rangle_\mathrm{e} \otimes \left(\mathrm{e}^{\mathrm{i}\theta_1}|\uparrow\uparrow\rangle_\mathrm{n} + \mathrm{e}^{\mathrm{i}\theta_2}|\downarrow\downarrow\rangle_\mathrm{n}\right),$$

and

$$|\xi'_2\rangle = |\mathrm{cc}\rangle_\mathrm{e} \otimes \left(\mathrm{e}^{\mathrm{i}\theta_1}|\uparrow\uparrow\rangle_\mathrm{n} + \mathrm{e}^{\mathrm{i}\theta_2}|\downarrow\downarrow\rangle_\mathrm{n}\right),$$

respectively by using a π pulse of ground-clock transition in the first atom (with an extra phase determined by the Rabi frequency) as shown around Eq. (24).

The above discussions are based on detecting ground-state atoms without losing the atoms. It was reported in Ref. [28] that high-fidelity (over 0.9999) measurement of strontium atoms can proceed with a survival probability over 0.999. Imaging AEL atoms with nuclear spins would require extra efforts. Recently, Ref. [40] demonstrated imaging of the ground-state ^{171}Yb atoms in tweezers with a fidelity about 0.997 and a loss probability around 2%–3% (near-unit fidelity can be achieved with larger atom loss probability).

6.2 Measurement of two atoms at a time in SBS

Measurement of two atoms can also lead to interesting states. For example, if no light is detected when measuring the two atoms initially in the state of Eq. (25), the state collapses to

$$|\Xi_1\rangle = \frac{1}{\sqrt{2}}|\mathrm{cc}\rangle_\mathrm{e} \otimes (|\uparrow\downarrow\rangle_\mathrm{n} + |\downarrow\uparrow\rangle_\mathrm{n}).$$

But if light is detected, and if it is possible to collect light scattered from the two nearby atoms when neither any device nor the environment knows which atom scatters the light, the state collapses to

$$|\Xi_2\rangle = \frac{1}{2}(|\mathrm{cg}\rangle_\mathrm{e} + |\mathrm{gc}_\mathrm{e}\rangle) \otimes (\mathrm{e}^{\mathrm{i}\theta_1}|\uparrow\uparrow\rangle_\mathrm{n} + \mathrm{e}^{\mathrm{i}\theta_2}|\downarrow\downarrow\rangle_\mathrm{n}),$$

which is a hyperentangled state where both the electronic states and the nuclear-spin states of the two atoms are maximally entangled [45]. Here, we need to emphasize that though it was not tested with AEL atoms for collecting light scattered from two atoms without distinguishing the light pathway, it is possible since the physical principle is similar to that of the Young's double-split experiment.

6.3 Measurement of $|\blacktriangle\rangle$

The three-atom state $|\blacktriangle\rangle$ in the form of Eq. (33) can also be used for creating interesting entangled states. Because of the descriptions shown above about SBS, we only briefly discuss the measurement of $|\blacktriangle\rangle$.

We first discuss the outcome of measuring one atom. If we measure the first atom and find light scattered, then Eq. (33) collapses to $|\mathrm{gcc}\rangle_\mathrm{e} \otimes (\mathrm{e}^{\mathrm{i}\vartheta_3}|\uparrow\uparrow\uparrow\rangle_\mathrm{n} + \mathrm{e}^{\mathrm{i}\vartheta_4}|\downarrow\downarrow\downarrow\rangle_\mathrm{n})/\sqrt{2}$. This state can be further converted to $|\mathrm{ccc}\rangle_\mathrm{e} \otimes (\mathrm{e}^{\mathrm{i}\vartheta_3}|\uparrow\uparrow\uparrow\rangle_\mathrm{n} + \mathrm{e}^{\mathrm{i}\vartheta_4}|\downarrow\downarrow\downarrow\rangle_\mathrm{n})/\sqrt{2}$ via the ground-clock transition in the first atom, which is the canonical GHZ state considering that the relative phase in it can be absorbed by defining new spin basis states as in Eq. (34). But if no light is scattered when measuring the first atom, the state collapses to

$$\begin{aligned}\frac{1}{2}\Big\{&\frac{\sqrt{6}}{2}|\mathrm{ccc}\rangle_\mathrm{e} \otimes \Big[\mathrm{e}^{\mathrm{i}\vartheta_1}\frac{|\uparrow\uparrow\downarrow\rangle_\mathrm{n} + |\uparrow\downarrow\uparrow\rangle_\mathrm{n} + |\downarrow\uparrow\uparrow\rangle_\mathrm{n}}{\sqrt{3}} \\ &+ \mathrm{e}^{\mathrm{i}\vartheta_2}\frac{|\uparrow\downarrow\downarrow\rangle_\mathrm{n} + |\downarrow\uparrow\downarrow\rangle_\mathrm{n} + |\downarrow\downarrow\uparrow\rangle_\mathrm{n}}{\sqrt{3}}\Big] \\ &+ \frac{|\mathrm{cgc}\rangle_\mathrm{e} + |\mathrm{ccg}\rangle_\mathrm{e}}{\sqrt{2}} \otimes \frac{\mathrm{e}^{\mathrm{i}\vartheta_3}|\uparrow\uparrow\uparrow\rangle_\mathrm{n} + \mathrm{e}^{\mathrm{i}\vartheta_4}|\downarrow\downarrow\downarrow\rangle_\mathrm{n}}{\sqrt{2}}\Big\}. \end{aligned} \quad (39)$$

Measurement of the second atom in the state of Eq. (39) can lead to two outcomes. (i) If no light is detected, then Eq. (39) collapses to the state where $\frac{1}{\sqrt{2}}(|\mathrm{cgc}\rangle_\mathrm{e} + |\mathrm{ccg}\rangle_\mathrm{e})$ in the last line of Eq. (39) is replaced by $|\mathrm{ccg}\rangle_\mathrm{e}$, and if we continue to measure the third atom, and detect light, then the state finally collapses to $|\mathrm{ccg}\rangle_\mathrm{e} \otimes (\mathrm{e}^{\mathrm{i}\vartheta_3}|\uparrow\uparrow\uparrow\rangle_\mathrm{n} + \mathrm{e}^{\mathrm{i}\vartheta_4}|\downarrow\downarrow\downarrow\rangle_\mathrm{n})/\sqrt{2}$. (ii) If light is detected, Eq. (39) collapses to $|\mathrm{cgc}\rangle_\mathrm{e} \otimes (\mathrm{e}^{\mathrm{i}\vartheta_3}|\uparrow\uparrow\uparrow\rangle_\mathrm{n} + \mathrm{e}^{\mathrm{i}\vartheta_4}|\downarrow\downarrow\downarrow\rangle_\mathrm{n})/\sqrt{2}$, which can be converted to the canonical GHZ state as discussed above.

We then discuss measuring three atoms at a time. We consider the case that we can collect light scattered from the atoms when neither any device nor the environment knows which atom scatters the light. If we find light scattered, Eq. (33) collapses to

$$\frac{1}{\sqrt{2}}|W\rangle_\mathrm{e} \otimes \left(\mathrm{e}^{\mathrm{i}\vartheta_3}|\uparrow\uparrow\uparrow\rangle_\mathrm{n} + \mathrm{e}^{\mathrm{i}\vartheta_4}|\downarrow\downarrow\downarrow\rangle_\mathrm{n}\right),$$

which is a hyerentangled state where the electronic state of the three atoms is in the maximally entangled W state, and the nuclear-spin state is in the maximally entangled GHZ state. In principle, it is possible to convert the electronic W state to the electronic GHZ state [60] so that the electronic GHZ state and the nuclear-spin GHZ state can simultaneously exist in three atoms.

7 Quantum dense coding with SBS

7.1 Dense coding model of Ref. [41]

It is known that Rydberg atoms are useful in quantum

computing (for a review, see, e.g., Refs. [46, 47, 61]), quantum simulation [62], and quantum optics [63]. In this section, we show a possible application of Rydberg atoms in the context of SBS in quantum dense coding [41]. Before presenting our quantum dense coding with SBS, it is useful to first review the original method of [41]. Consider two qubits, each with two qubit states $|0\rangle$ and $|1\rangle$, then we can have four Bell states in the two qubits,

$$\begin{aligned}
|\mathbb{B}_1\rangle &= (|10\rangle - |01\rangle)/\sqrt{2},\\
|\mathbb{B}_2\rangle &= (|10\rangle + |01\rangle)/\sqrt{2},\\
|\mathbb{B}_3\rangle &= (|11\rangle - |00\rangle)/\sqrt{2},\\
|\mathbb{B}_4\rangle &= (|11\rangle + |00\rangle)/\sqrt{2}.
\end{aligned} \tag{40}$$

We consider single-qubit gates represented by $\hat{I}, \hat{X}, \hat{Y}, \hat{Z}$, where $\hat{I}$ is the identity, $\hat{X}$ and $\hat{Z}$ are the first and third Pauli matrices, and $\hat{Y} = \mathrm{i}\sigma_y$. By $\hat{X}\{|0\rangle, |1\rangle\} = \{|1\rangle, |0\rangle\}$, $\hat{Y}\{|0\rangle, |1\rangle\} = \{|1\rangle, -|0\rangle\}$, and $\hat{Z}\{|0\rangle, |1\rangle\} = \{-|0\rangle, |1\rangle\}$, one can examine that by applying these gates to the first qubit in $|\mathbb{B}_1\rangle$, the four states in Eq. (40) transform to $|\mathbb{B}_1\rangle, -|\mathbb{B}_3\rangle, -|\mathbb{B}_4\rangle$, and $|\mathbb{B}_2\rangle$, respectively. Dense coding proceeds with four steps. First, somebody prepares, e.g., $|\mathbb{B}_1\rangle$, and sends the two qubits to two persons named, e.g., Alice and Bob. Second, Bob applies one of the four single-qubit gates on his bit, where he does nothing if he chooses the identity. Third, Bob sends his qubit to Alice via a public channel. Fourth, Alice measures the state of the two qubits to determine which of the four single-qubit gates Bob used to rotate the qubit Alice just received. Because the four Bell states in Eq. (40) are orthogonal to each other, it is possible for Alice to distinguish the four Bell states. If Alice and Bob already agreed with each other before the above mentioned four steps that the four operations $\hat{I}, \hat{X}, \hat{Y}, \hat{Z}$ represent binary series 00, 01, 10, and 11, respectively, then the above procedure is one example for Bob to send information of two bits when actually one qubit is sent to Alice. Note that the nature of quantum mechanics guarantees that when an eavesdropper tries to gain knowledge about the qubit Bob sends to Alice via the public channel, Alice can find it out and then can discard that qubit from Bob.

7.2 Dense coding with SBS

Before presenting the quantum dense coding with SBS, we note that by using single-qubit gates or redefinition of basis states as in Eq. (21), we can prepare the following SBS

$$|SB1\rangle \equiv \frac{1}{\sqrt{2}}\Big(|\mathrm{cc}\rangle_\mathrm{e} \otimes |\Phi\rangle_\mathrm{n} + |\Phi\rangle_\mathrm{e} \otimes |\Psi\rangle_\mathrm{n}\Big) \tag{41}$$

via the protocol of Section 4, where

$$\begin{aligned}
|\Phi\rangle_\mathrm{e} &= \frac{|\mathrm{cg}\rangle_\mathrm{e} + |\mathrm{gc}\rangle_\mathrm{e}}{\sqrt{2}},\\
|\Phi\rangle_\mathrm{n} &= \frac{|\uparrow\downarrow\rangle_\mathrm{n} + |\downarrow\uparrow\rangle_\mathrm{n}}{\sqrt{2}},\\
|\Psi\rangle_\mathrm{n} &= \frac{|\uparrow\uparrow\rangle_\mathrm{n} + |\downarrow\downarrow\rangle_\mathrm{n}}{\sqrt{2}}.
\end{aligned} \tag{42}$$

By using single-qubit nuclear-spin gates $\{\hat{I}_\mathrm{n}, \hat{X}_\mathrm{n}, \hat{Y}_\mathrm{n}, \hat{Z}_\mathrm{n}\}$ for the first atom, $|\Phi\rangle_\mathrm{n}$ becomes $\{|\Phi\rangle_\mathrm{n}, |\Psi\rangle_\mathrm{n}, |\Psi\rangle'_\mathrm{n}, |\Phi\rangle'_\mathrm{n}\}$, respectively, where

$$\begin{aligned}
|\Phi\rangle'_\mathrm{n} &= \frac{|\uparrow\downarrow\rangle_\mathrm{n} - |\downarrow\uparrow\rangle_\mathrm{n}}{\sqrt{2}},\\
|\Psi\rangle'_\mathrm{n} &= \frac{|\uparrow\uparrow\rangle_\mathrm{n} - |\downarrow\downarrow\rangle_\mathrm{n}}{\sqrt{2}},
\end{aligned} \tag{43}$$

while $|\Psi\rangle_\mathrm{n}$ becomes $\{|\Psi\rangle_\mathrm{n}, |\Phi\rangle_\mathrm{n}, |\Phi\rangle'_\mathrm{n}, |\Psi\rangle'_\mathrm{n}\}$, respectively. Bob can also apply one among the two possible operations $\{\hat{I}_\mathrm{e}, \hat{X}_\mathrm{e}\}$ on the electronic state space in the first atom. When $\hat{X}_\mathrm{e}$ is used, $|\mathrm{cc}\rangle_\mathrm{e}$ and $|\Phi\rangle_\mathrm{e}$ become $|\mathrm{gc}\rangle_\mathrm{e}$ and $|\Psi\rangle_\mathrm{e} = \frac{|\mathrm{gg}\rangle_\mathrm{e} + |\mathrm{cc}\rangle_\mathrm{e}}{\sqrt{2}}$, respectively. For brevity, we list the operations used for the first atom and the resulting super Bell states,

$$\begin{aligned}
&\hat{I}_\mathrm{e}\hat{I}_\mathrm{n} : |SB1\rangle,\\
&\hat{I}_\mathrm{e}\hat{X}_\mathrm{n} : |SB2\rangle \equiv \frac{1}{\sqrt{2}}\Big(|\mathrm{cc}\rangle_\mathrm{e} \otimes |\Psi\rangle_\mathrm{n} + |\Phi\rangle_\mathrm{e} \otimes |\Phi\rangle_\mathrm{n}\Big),\\
&\hat{I}_\mathrm{e}\hat{Y}_\mathrm{n} : |SB3\rangle \equiv \frac{1}{\sqrt{2}}\Big(|\mathrm{cc}\rangle_\mathrm{e} \otimes |\Psi\rangle'_\mathrm{n} + |\Phi\rangle_\mathrm{e} \otimes |\Phi\rangle'_\mathrm{n}\Big),\\
&\hat{I}_\mathrm{e}\hat{Z}_\mathrm{n} : |SB4\rangle \equiv \frac{1}{\sqrt{2}}\Big(|\mathrm{cc}\rangle_\mathrm{e} \otimes |\Phi\rangle'_\mathrm{n} + |\Phi\rangle_\mathrm{e} \otimes |\Psi\rangle'_\mathrm{n}\Big),\\
&\hat{X}_\mathrm{e}\hat{I}_\mathrm{n} : |SB5\rangle \equiv \frac{1}{\sqrt{2}}\Big(|\mathrm{gc}\rangle_\mathrm{e} \otimes |\Phi\rangle_\mathrm{n} + |\Psi\rangle_\mathrm{e} \otimes |\Psi\rangle_\mathrm{n}\Big),\\
&\hat{X}_\mathrm{e}\hat{X}_\mathrm{n} : |SB6\rangle \equiv \frac{1}{\sqrt{2}}\Big(|\mathrm{gc}\rangle_\mathrm{e} \otimes |\Psi\rangle_\mathrm{n} + |\Psi\rangle_\mathrm{e} \otimes |\Phi\rangle_\mathrm{n}\Big),\\
&\hat{X}_\mathrm{e}\hat{Y}_\mathrm{n} : |SB7\rangle \equiv \frac{1}{\sqrt{2}}\Big(|\mathrm{gc}\rangle_\mathrm{e} \otimes |\Psi\rangle'_\mathrm{n} + |\Psi\rangle_\mathrm{e} \otimes |\Phi\rangle'_\mathrm{n}\Big),\\
&\hat{X}_\mathrm{e}\hat{Z}_\mathrm{n} : |SB8\rangle \equiv \frac{1}{\sqrt{2}}\Big(|\mathrm{gc}\rangle_\mathrm{e} \otimes |\Phi\rangle'_\mathrm{n} + |\Psi\rangle_\mathrm{e} \otimes |\Psi\rangle'_\mathrm{n}\Big).
\end{aligned} \tag{44}$$

The eight super Bell states are orthogonal to each other, so they can be distinguished in experiments in principle and can represent the binary numbers $\{000, 001, 010, 011, 100, 101, 110, 111\}$. Like Section 7.1, quantum dense coding with SBS also needs four steps as described there. The difference with SBS lies in that Alice and Bob agree beforehand that the eight different operations correspond to the eight binary numbers. Then, by sending only one atom to Alice, Bob conveys three bits of classical information.

As light can carry quantum information while flying a long distance, we will discuss the possibility to map the entanglement from atoms to photons so as to realize dense coding for long-distance communication.

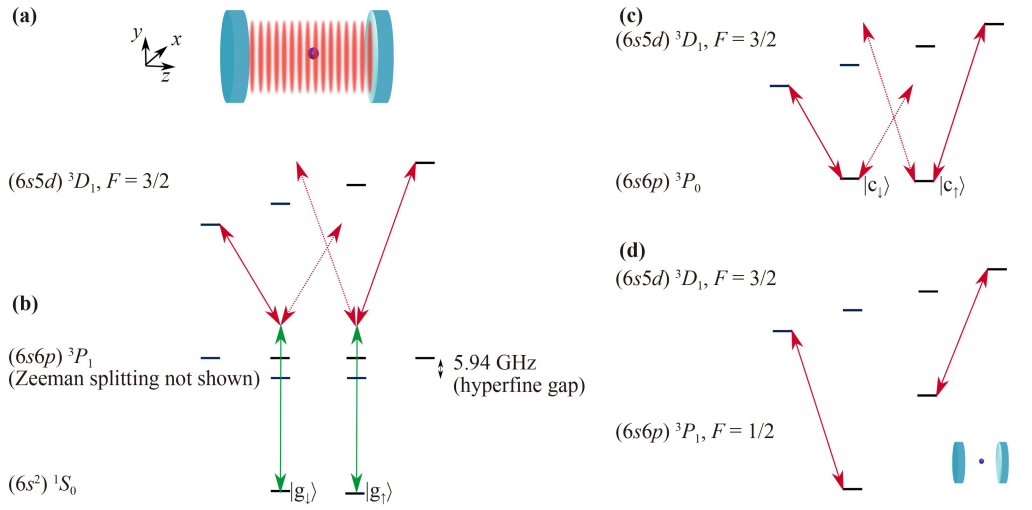

Fig. 10 Scheme for mapping atomic states to photons. **(a)** An atom is placed inside a Fabry–Perot resonator. The quantization axis is along z specified by an external magnetic field B_z. Laser fields sent along x or y directions can couple the ground or clock states of the atoms to $6s5d\,^3D_1, F = 3/2$. **(b)** The two ground Zeeman substates $|g_\uparrow\rangle$ and $|g_\downarrow\rangle$ are coupled to the $m_F = 3/2$ and $m_F = -3/2$ states of $6s5d\,^3D_1, F = 3/2$ via the intermediate state $6s6p\,^3P_1$. The detuning at $6s6p\,^3P_1$ is large compared to the Zeeman splitting which is not shown in the figure. The lower transition is with a z-polarized field, and the upper field is x-polarized. The dashed arrows show transitions largely detuned so that no transition occurs there. **(c)** The two nuclear-spin substates $|c_\uparrow\rangle$ and $|c_\downarrow\rangle$ are coupled to the $m_F = 3/2$ and $m_F = -3/2$ states of $6s5d\,^3D_1, F = 3/2$. Dashed arrows indicate detuned transitions where no population transfer occurs. **(d)** The cavity mode is nearly resonant with the transition $6s5d\,^3D_1, F = 3/2 \leftrightarrow 6s6p\,^3P_1, F = 1/2$, in which the g factor of the lower state is nearly six times that of the upper state, and the Zeeman splitting between the two transitions indicated by the two arrows is about $\mu_B B$, which is supposed to be small compared to the cavity linewidth. We assume that the cavity photon is coupled almost perfectly to an optical fibre which is not shown here. Mapping of the the SBS state of atoms to that of photons proceeds as follows. (i) Move the two atoms to two cavities; (ii) The processes in (b) and (d) map the nuclear-spin states in the ground-state atoms to polarization qubits of photons; (iii) Use (c) and (d) to map the nuclear-spin states in the clock-state atoms to polarization qubits of photons. Because of the time gap between the steps (ii) and (iii), the "g" and "c" degree of freedom of atoms is mapped to the time-bin degree of freedom of photons.

7.3 Mapping atomic entanglement to photons

Sending information via photons can enable long-distance quantum communication. If SBS of the atomic state is mapped to a super Bell state of photons, then the dense coding of Section 7.2 can proceed as follows. First, map the entanglement from the two atoms to two photons, where the "c" and "g" electronic qubit states of atoms are mapped to the time-bin qubit states of photons, and the up and down nuclear-spin qubit states of atoms are mapped to the polarization-encoded qubit states of photons. Second, the two photons are sent to Alice and Bob, respectively. Third, Bob performs one of the eight operations on his photon in a way similar to those for atoms shown in Eq. (44). Fourth, Bob sends his photon to Alice. Fifth, Alice performs measurement to check whether the two-photon state is one of the eight super Bell states. If not, an eavesdropper ever tried to observe the photonic state Bob sent to her, so Alice can discard the photons; if yes, Alice can determine the three-digit binary number Bob meant to send according to her measurement result. By this, Alice can receive three bits of classical information when only one photon is sent by Bob.

We consider the mapping outlined in Fig. 10. (i) Move the two entangled atoms into two separate cavities, each of which is coupled to a fibre with a high efficiency. Note that the coherent transport of atoms while preserving the internal states was experimentally possible [16]. (ii) Use two sets of two-photon laser fields to realize

$$|g_\uparrow\rangle \to |[6s5d\,^3D_1]F = 3/2, m_F = 3/2\rangle, \tag{45}$$

$$|g_\downarrow\rangle \to |[6s5d\,^3D_1]F = 3/2, m_F = -3/2\rangle, \tag{46}$$

where both sets of fields are via the intermediate state $6s6p\,^3P_1$ but with different detunings at it so that the two fields for the transition of Eq. (45) and the two fields for the transition of Eq. (46) are independent with each other. The transitions $6s6p\,^1S_0 \to 6s6p\,^3P_1$ and $6s6p\,^3P_1 \to 6s5d\,^3D_1$ are with dipole matrix elements about $0.2a_0e$ (which includes a factor due to the spin-orbit coupling [37]) and $1.6a_0e$ [64], respectively. This makes it possible to realize large Rabi frequencies for Eqs. (45) and (46). However, we do not need to have large Rabi frequencies, and one can tune the fields to be near to $[6s6p\,^3P_1]F = 3/2$ as in Ref. [20]. In this case, the $[6s6p\,^3P_1]F = 1/2$ hyperfine level, which is about 6 GHz

away from the $F=3/2$ level [37], does not participate in the transitions of Eqs. (45) and (46). (iii) The cavity field is near resonant with the transition $[6s5d\,^3D_1]F=3/2 \leftrightarrow [6s6s\,^3P_1]F=1/2$. As a result, the state in Eq. (45) can lead to an emission of σ^+ polarized photon, while the state of Eq. (46) can lead to an emission of σ^- polarized photon. The photons are coupled to optical fibres and sent to Alice and Bob, respectively. (iv) Use two sets of UV laser fields to realize

$$|c_\uparrow\rangle \rightarrow |[6s5d\,^3D_1]F=3/2, m_F=3/2\rangle, \tag{47}$$

$$|c_\downarrow\rangle \rightarrow |[6s5d\,^3D_1]F=3/2, m_F=-3/2\rangle. \tag{48}$$

(v) As in step (iii), the two states in Eqs. (47) and (48) lead to emission of cavity photons of different polarizations, which are further coupled to fibres and sent to Alice and Bob, respectively. Because there is time difference between steps (iii) and (v), the "c"–"g" electronic degree of freedom is mapped to the time-bin degree of freedom. Here, we only show the basic process for mapping the atomic SBS to photonic SBS. In practice, one can use adiabatic passage process to realize the mapping as experimentally realized in Ref. [65].

We note that high-fidelity transport of neutral atoms while preserving the atoms and their internal state is not trivial [16], and the collection of photons emitted from the cavities with high efficiency also needs efforts. Therefore it is a demanding task to realize a photonic SBS with a high fidelity. On the other hand, the basic elements to realize the novel quantum dense coding can be tested with the atomic SBS with the single-qubit operations of Eq. (44).

8 Discussion

Here, we summarize the mechanism introduced in this paper for the novel entanglement protocols, and compare the theory shown here and the previous results published about the quantum control over nuclear-spin qubits in divalent neutral atoms. We also discuss the gate speed, magnetic field used in the protocols, and connections with experiments in hope to stimulate further explorations.

8.1 Creation of unit Rydberg excitation in detuned Rabi oscillations

The fast nuclear-spin gates presented in Sections 2 and 3, and the exotic electrons–nuclei entanglement in Sections 4 and 5 rely on two methods to create unit Rydberg excitation among two atoms when there are both laser detuning and Rydberg blockade.

For the nuclear-spin gates in Sections 2 and 3, the novel mechanism used is that when a common laser field is sent to two nearby atoms in the initial state, as an example, $|c_\uparrow c_\downarrow\rangle$, with the laser tuned to the middle between the two clock-Rydberg transitions of Fig. 1, we have the following transition in the strong blockade limit,

$$|r_+ c_\downarrow\rangle \xleftarrow{\text{detuned by } \Delta} |c_\uparrow c_\downarrow\rangle \xrightarrow{\text{detuned by } -\Delta} |c_\uparrow r_-\rangle. \tag{49}$$

If the left transition in Eq. (49) is absent, one can prove [51] that there can never be unit Rydberg population, i.e., the state $|c_\uparrow r_-\rangle$ will not be fully populated. Likewise, if the right transition in Eq. (49) is absent,the state $|r_+ c_\downarrow\rangle$ can not be fully populated either. A novel mechanism used here is that, it is possible to realize a unit Rydberg excitation starting from the state $|c_\uparrow c_\downarrow\rangle$ when Eq. (49) is realized in the blockade condition. In other words, it is possible to create one Rydberg excitation even though neither $|r_+ c_\downarrow\rangle$ nor $|c_\uparrow r_-\rangle$ is resonantly excited. This surprising mechanism is in sharp contrast to the usually employed creation of unit Rydberg excitation via resonant laser excitation of two nearby atoms [3, 19]. By the symbols used in this paper, the method of Refs. [3, 19] relies on exciting

$$|r_+ c_\uparrow\rangle \xleftarrow{\text{resonant}} |c_\uparrow c_\uparrow\rangle \xrightarrow{\text{resonant}} |c_\uparrow r_+\rangle \tag{50}$$

in the strong blockade condition so that the state $(|r_+ c_\uparrow\rangle + |c_\uparrow r_+\rangle)/\sqrt{2}$ can be created, i.e., unit Rydberg excitation among two atoms is achieved. Unit Rydberg excitation was useful for creating maximal entanglement between atoms [3, 19], which is why in this paper we explore the creation of unit Rydberg excitation via the novel method of Eq. (49).

The electrons–nuclei entanglement in Sections 4 and 5 is realized via another method for creating unit Rydberg excitation in detuned transitions with Rydberg blockade. In practice, it was known that by

$$|r_+ c_\uparrow\rangle \xleftarrow{\text{detuned by } \Delta} |c_\uparrow c_\uparrow\rangle \xrightarrow{\text{detuned by } \Delta} |c_\uparrow r_+\rangle \tag{51}$$

with a constant Rabi frequency, there can be no unit Rydberg excitation [38, 51]. But Sections 4 and 5 show that if we change the Rabi frequency though the laser frequency is constant, it is possible to create unit Rydberg excitation among the two atoms. The simplest case is to use two laser pulses where the Rabi frequency in the second pulse differs from that in the first pulse in a certain way as in Sections 4 and 5. By this method, it is possible to create the state $(|r_+ c_\uparrow\rangle + |c_\uparrow r_+\rangle)/\sqrt{2}$ from $|c_\uparrow c_\uparrow\rangle$ even though the lasers are detuned during the excitation process. Importantly, the same unit excitation can be realized if Δ is replaced by $-\Delta$, which means that it fits perfectly for the nuclear-spin qubits studied in this paper.

8.2 Comparison with other entanglement of divalent atoms via Rydberg blockade

It is useful to compare the theory in this paper with

other Rydberg-mediated entanglement in electronic state space [19, 21, 22] or nuclear-spin state space [20, 23, 35, 37, 66] of divalent atoms.

First, this paper studies entanglement between electrons and nuclear spin states in divalent atoms, while other papers studied entanglement between nuclear spins [20, 23, 35, 37], or entanglement between electrons [19, 21, 22]. Reference [45] studied simultaneous entanglement between electrons and entanglement between nuclear spins of two atoms, but the hyperentangled state there doesn't contain entanglement between electrons and nuclear spins.

Second, for the entanglement protocols relying on unit Rydberg population [19, 37, 45], a resonant ground-Rydberg [37, 45] or clock-Rydberg [19, 45] transition was employed in the blockade condition. The theory in this paper relies on off-resonant ground- or clock-Rydberg transition. To the best of our knowledge, this novel mechanism was not reported.

Third, for nuclear-spin entanglement with experimental demonstration [20, 23] or theoretical analysis [66], either the gate of [11] via dynamical phases in detuned Rabi cycles [38] was employed, or the gate via optimal control was used [23]. Theses methods, however, fit well for hyperfine qubits in alkali-metal atoms or optical clock qubits of AEL atoms [47]. In AEL atoms with nuclear spins, the frequency separation between the nuclear-spin qubit states in ground or clock state is negligible compared to a MHz-scale Rydberg Rabi frequency in a Gauss-scale magnetic field as frequently used in experiments. To use the methods designed for hyperfine qubits or optical clock qubits [47] with nuclear-spin qubits, one can enlarge the ratio between the Zeeman splitting of nearby Rydberg Zeeman substates and the Rydberg Rabi frequency so as to avoid the Rydberg excitation of the nontarget nuclear spin state as done in Refs. [20, 23]. This, however, strongly limits the gate speed which may explain why using similar optimal-control protocols, the gate of Ref. [18] with hyperfine qubits has a higher fidelity than that of Ref. [23] with nuclear-spin qubits. These methods differ from the theory in this paper in two aspects. (i) The theory here does not purely rely on dynamical phases for entanglement though it uses detuned Rabi cycles. For example, the nuclear-spin gate in Sections 2 and 3 realizes a controlled-β gate when the last laser pulse has a relative phase β, while the gate in Section 3 realizes a controlled-β gate when the last laser pulse has a relative phase β plus another phase due to a rotating frame transform. These are in sharp contrast to the method of Refs. [11, 38], where it was shown in Ref. [47] that the protocol of Ref. [11] can be used to realize a controlled-β gate with an arbitrary β, but there is no linear relation between β and the laser phases. (ii) The theory here is designed for nuclear-spin qubits in divalent atoms with nuclear spins, so it works well for nuclear-spin qubits while not so for hyperfine qubits of alkali metals or optical clock qubits of AEL atoms [47]. Our theory relies on exciting the two qubit states to Rydberg states off-resonantly, which fits perfectly the nuclear-spin qubits in a Gauss-scale magnetic field. As a result, the Rydberg Rabi frequency is comparable to the Zeeman splitting of two nearby Rydberg Zeeman substates, which ensures fast gate speeds. In other words, when fixing the magnetic field, the achievable gate speed with the theory in this paper will be larger than those in [20, 23] for realizing nuclear-spin entanglement in divalent atoms.

8.3 Gate speed

The speed of our nuclear-spin quantum gates is large. To discuss the speed of a Rydberg-mediated quantum gate, it is useful to denote the gate duration in terms of $\pi/\Omega_{\rm m}$ where $\Omega_{\rm m}$ is the maximal Rabi frequency during the protocol. To our knowledge, the fastest Rydberg-blockade-based entangling gate that can be transferred to the CZ gate via single-qubit gates needed two laser pulses of total duration about $2.732\pi/\Omega_{\rm m}$ [11] without using optimal control, or about $2.414\pi/\Omega_{\rm m}$ [18] by optimal control. The gates of [11, 18] depend on exciting only one of the two qubit states to Rydberg states, which means that it fits qubits defined either by the hyperfine substates as used in the experiments of Refs. [11, 16, 17] or by the optical clock qubits (there was an experiment [21] with the optical clock qubits via another gate protocol [67]). Of course, one can try to use it for nuclear spin qubits as experimentally done in Refs. [20, 23] with a $\Omega_{\rm m}$ small compared to the Zeeman splitting between Rydberg states. The small $\Omega_{\rm m}$ results in relatively long gate duration, which was possibly why the gate fidelity of Ref. [20] was smaller than that of Ref. [11], and that of Ref. [23] was smaller than that of Ref. [18] though in principle AEL atoms can allow high-fidelity entanglement generation [19, 22] due to the advantages possessed by them as introduced in Section 1. In this paper, the two or three-pulse gate has a total duration $2.589\pi/\Omega_{\rm m}$ or $5.054\pi/\Omega_{\rm m}$. With $\Omega_{\rm m}/(2\pi) = 13$ MHz realizable [19], even the slower three-pulse gate in this paper would have a short duration 0.19 μs. This gives hope to realize fast and high-fidelity nuclear-spin entanglement.

8.4 Magnetic field

The theory shown in this paper is based on using a magnetic field below 10 G for specifying the quantization axis of the atoms. The numerical simulations for the nuclear-spin quantum gates shown in Figs. 2, 3, 4, and 5 assume $2\Delta/(2\pi) \approx 4$ MHz, which corresponds to a B-field of about 2 G. For the data of SBS shown in Figs. 6 and 7, the Zeeman splitting is $2\Delta/(2\pi) \approx 2.8$ MHz which corresponds to $B \approx 1.5$ G. For the data about $|\blacktriangle\rangle$ shown in Figs. 8 and 9, the field $B \approx 1.7$ G is assumed. If Rabi

frequencies used in them are increased by three times which can lead to much faster entanglement generations with higher fidelities, B-fields below 10 G are still sufficient. So, the protocols in this paper are compatible with recent experimental facilities studying nuclear spins, where a B-field of 4.11 G [20], 5 G [23], 11 G [39], or a value in the range (0, 18] G [40] was used with ^{87}Sr [39] or ^{171}Yb [20, 23, 40]. These bring hope to realize functional quantum devices with nuclear-spin quantum memories [30, 31, 34, 35, 45, 66].

8.5 Application with other atomic species

The numerical simulations in this paper are performed with ^{171}Yb for it can simplify the analysis due to that it has the simplest nuclear spin $I = 1/2$. Extending the theory to isotopes with larger I is possible. For example, for nuclear-spin qubits defined with $1 - I$ and $-I$ in ^{87}Sr, the ground-Rydberg transition was demonstrated [39], and the clock-Rydberg transition was demonstrated with ^{88}Sr [19, 22]. Moreover, when the Rydberg Rabi frequencies for the two nuclear spin states do not have the same magnitude as in ^{171}Yb shown in Eq. (6), application of the theory in this paper may lead to more exotic entanglement because different Rydberg excitation rates in the two qubit states of each atom can result in different dynamics useful for quantum control [57]. In general, we expect the entanglement protocols to be useful for divalent atoms with nuclear spins and metastable clock states, such as calcium, barium, zinc, cadmium, and mercury [33].

8.6 Connections with experiments

The protocols introduced in this paper rely on techniques intimately related with recent experiments.

The fast clock-Rydberg transition assumed throughout this paper can be experimentally realized. In Ref. [19], Rabi frequencies about $2\pi \times 6.8$ MHz were used to excite the clock state to $5s61s\ ^3S_1$ of ^{88}Sr. The two atoms to be entangled were separated by about 3.6 μm and experienced the same laser fields in Ref. [19]. In Ref. [21], time-dependent Rabi frequencies up to $2\pi \times 18$ MHz were used for the transition from the clock state to $5s40d\ ^3D_1$ of ^{88}Sr, and short atomic separation 1.2 μm was employed. This setting with very short atomic separation fits well for our theory since each Rydberg excitation should occur for the two or three atoms simultaneously. For the state $|\blacktriangle\rangle$ where three atoms should be close enough, the experiment of Ref. [18] placed three atoms with an atom–atom separations of only 2 μm in triangular gate sites, where the triangular configuration enabled strong, symmetric interactions between three qubits. These point to the experimental feasibility of the protocols here.

The ground-Rydberg transition via a low-lying intermediate state was possible. In Ref. [20], the Rydberg state $6s74s\ ^3S_1$ was excited from the ground state of ^{171}Yb for entangling nuclear spin states in the ground state. The Rydberg Rabi frequency was $2\pi \times 0.763$ MHz so as to avoid the excitation of the nontarget nuclear spin state as required by the protocol used in [20]. However, it was analyzed in Ref. [37] that Rabi frequencies over $2\pi \times 1$ MHz for exciting states with principal number around 70 is feasible.

The fast shifting of energy of Rydberg states required in Section 3 is experimentally feasible. There are two possible approaches to shifting the transition energy between the Rydberg state and the clock or ground state. First, one can shift the energy of the atomic states by exciting the outer valence electron. In Ref. [39], two nuclear spin qubit states with $m_I = -I, 1 - I$ in ^{87}Sr were isolated via Stark shifting other nuclear spin states away from the resonant beams. In Ref. [40], light shifts in excited states were used to coherently control the nuclear spin states in ^{171}Yb. Second, the excitation of the inner valence electron of Rydberg states can be used. For example, energy shifts over $2\pi \times 10$ MHz were demonstrated for both the $(6s6n)^3S_1$ [48] and the $(6s6n)^1S_0$ [68] Rydberg states via the excitation of the $Yb^+ 6s \to 6p_{1/2}$ transition of the inner valence electron in ^{174}Yb. Extending the methods of Refs. [48, 68] to ^{171}Yb would require calibrating polarization dependence of light shifts as in [39, 40].

9 Conclusions

We present fast and high-fidelity nuclear-spin controlled-phase gates of an arbitrary phase in AEL atoms. By exciting two AEL atoms with global laser fields where both nuclear spin qubit states of each atom are Rydberg excited, a controlled-phase gate of an arbitrary phase can be realized via three laser pulses of total duration $5.05\pi/\Omega_{\rm m}$, where $\Omega_{\rm m}$ is the largest Rydberg Rabi frequency during the pulses. We also show that if spin-dependent Stark shift ($\sim \Omega_{\rm m}$) is realizable, the same gate can be realized with two laser pulses of total duration $2.59\pi/\Omega_{\rm m}$. With large $\Omega_{\rm m}$ for the transition between the clock and Rydberg states of AEL realizable as recently demonstrated in experiments, and concerning that fast gates are easier to attain a higher fidelity in practice, the protocols can enable high-fidelity entanglement in nuclear spins of AEL atoms.

We also present two protocols to entangle electrons and nuclear spins in AEL. First, we show a super Bell state (SBS) entangled between the electrons and nuclei of two atoms. SBS is like a large "Bell" state entangled between three "small" Bell states and one product state. For three atoms, we show a protocol to realize a highly entangled state that includes W and GHZ states simultaneously. These two multi-atom entangling protocols

have durations $7.69\pi/\Omega_{\rm m}$ and $11.4\pi/\Omega_{\rm m}$, respectively, and can be used for preparing Bell, hyperentangled, and nuclear-spin GHZ states based on measurement. SBS can also enable dense coding where three classical bits of information can be securely shared when only one physical particle is sent in a public channel.

Acknowledgements The author thanks Yan Lu for useful discussions. This work was supported by the National Natural Science Foundation of China under Grant Nos. 12074300 and 11805146, the Innovation Program for Quantum Science and Technology 2021ZD0302100, and the Fundamental Research Funds for the Central Universities.

Appendix A: Hamiltonians for generating the nuclear-spin gate

With π polarized laser fields, the projection of the atomic angular momentum is conserved, so that the dynamics of the atomic states can be specified by the total m_F of the initial two-atom state. For $|{\rm c}_\uparrow{\rm c}_\uparrow\rangle \equiv |{\rm cc}\rangle_{\rm e}\otimes|\uparrow\uparrow\rangle_{\rm n}$, the Hamiltonian is

$$\hat{H}_{\uparrow\uparrow}=\begin{pmatrix} V+2\Delta & \frac{\Omega_{{\rm c}\uparrow}}{2} & \frac{\Omega_{{\rm c}\uparrow}}{2} & 0\\ \frac{\Omega^*_{{\rm c}\uparrow}}{2} & \Delta & 0 & \frac{\Omega_{{\rm c}\uparrow}}{2}\\ \frac{\Omega^*_{{\rm c}\uparrow}}{2} & 0 & \Delta & \frac{\Omega_{{\rm c}\uparrow}}{2}\\ 0 & \frac{\Omega^*_{{\rm c}\uparrow}}{2} & \frac{\Omega^*_{{\rm c}\uparrow}}{2} & 0 \end{pmatrix} \tag{A1}$$

in the basis of

$$\{|r_+r_+\rangle, |r_+{\rm c}_\uparrow\rangle, |{\rm c}_\uparrow r_+\rangle, |{\rm c}_\uparrow{\rm c}_\uparrow\rangle\}.$$

For $|{\rm c}_\downarrow{\rm c}_\downarrow\rangle \equiv |{\rm cc}\rangle_{\rm e}\otimes|\downarrow\downarrow\rangle_{\rm n}$, the Hamiltonian is

$$\hat{H}_{\downarrow\downarrow}=\begin{pmatrix} V-2\Delta & \frac{\Omega_{{\rm c}\downarrow}}{2} & \frac{\Omega_{{\rm c}\downarrow}}{2} & 0\\ \frac{\Omega^*_{{\rm c}\downarrow}}{2} & -\Delta & 0 & \frac{\Omega_{{\rm c}\downarrow}}{2}\\ \frac{\Omega^*_{{\rm c}\downarrow}}{2} & 0 & -\Delta & \frac{\Omega_{{\rm c}\downarrow}}{2}\\ 0 & \frac{\Omega^*_{{\rm c}\downarrow}}{2} & \frac{\Omega^*_{{\rm c}\downarrow}}{2} & 0 \end{pmatrix} \tag{A2}$$

in the basis of

$$\{|r_-r_-\rangle, |r_-{\rm c}_\downarrow\rangle, |{\rm c}_\downarrow r_-\rangle, |{\rm c}_\downarrow{\rm c}_\downarrow\rangle\}.$$

For $|{\rm c}_\uparrow{\rm c}_\downarrow\rangle \equiv |{\rm cc}\rangle_{\rm e}\otimes|\uparrow\downarrow\rangle_{\rm n}$, the Hamiltonian is

$$\hat{H}_{\uparrow\downarrow}=\begin{pmatrix} V & \frac{\Omega_{{\rm c}\downarrow}}{2} & \frac{\Omega_{{\rm c}\uparrow}}{2} & 0\\ \frac{\Omega^*_{{\rm c}\downarrow}}{2} & \Delta & 0 & \frac{\Omega_{{\rm c}\uparrow}}{2}\\ \frac{\Omega^*_{{\rm c}\uparrow}}{2} & 0 & -\Delta & \frac{\Omega_{{\rm c}\downarrow}}{2}\\ 0 & \frac{\Omega^*_{{\rm c}\uparrow}}{2} & \frac{\Omega^*_{{\rm c}\downarrow}}{2} & 0 \end{pmatrix} \tag{A3}$$

in the basis of

$$\{|r_+r_-\rangle, |r_+{\rm c}_\downarrow\rangle, |{\rm c}_\uparrow r_-\rangle, |{\rm c}_\uparrow{\rm c}_\downarrow\rangle\},$$

while for $|{\rm c}_\downarrow{\rm c}_\uparrow\rangle \equiv |{\rm cc}\rangle_{\rm e}\otimes|\downarrow\uparrow\rangle_{\rm n}$, the Hamiltonian is similar to Eq. (A3).

Appendix B: Frame transform

Here, we show the details about a frame transform in the analyses for creating SBS. The description from Section 4.1.1 to Section 4.1.2 is in a rotating frame that transforms the Hamiltonian $\hat{\mathbb{H}}$ to ${\rm e}^{{\rm i}t\hat{R}}\hat{\mathbb{H}}{\rm e}^{-{\rm i}t\hat{R}}-\hat{R}\equiv\hat{H}$ with

$$\hat{R}=\omega(|r_+\rangle\langle r_+|+|r_-\rangle\langle r_-|)-\omega_{\rm gc}(|{\rm g}_\uparrow\rangle\langle{\rm g}_\uparrow|+|{\rm g}_\downarrow\rangle\langle{\rm g}_\downarrow|),$$

where $\omega\pm\Delta=E_\pm$ is the energy separation (divided by the reduced Planck constant) between the clock state and $|r_\pm\rangle$, and $\omega_{\rm gc}$ is the energy separation between the ground and clock states; the energy is measured in reference to that of the clock state, and we ignore the energy separation between $|{\rm c}_\uparrow\rangle$ and $|{\rm c}_\downarrow\rangle$ and that between $|{\rm g}_\uparrow\rangle$ and $|{\rm g}_\downarrow\rangle$ since they are orders of magnitude smaller than the Rabi frequencies considered in this paper due to the tiny nuclear-spin Zeeman splitting in a Gauss-scale magnetic field. In the third pulse shown below, another rotating frame defined with

$$\begin{aligned}\hat{R}'=&E_+|r_+\rangle\langle r_+|+E_-|r_-\rangle\langle r_-|)\\&-\omega_{\rm gc}(|{\rm g}_\uparrow\rangle\langle{\rm g}_\uparrow|+|{\rm g}_\downarrow\rangle\langle{\rm g}_\downarrow|)\end{aligned}$$

is used. The frame transform from $\hat{R}$ to $\hat{R}'$ changes the phase α in the first two equations of Eq. (17) to

$$\alpha'=\alpha+\Delta\left(\mathbb{T}^{({\rm S})}_{\rm p1}+\mathbb{T}^{({\rm S})}_{\rm p2}\right).$$

Appendix C: Hamiltonians in the third pulse for creating SBS

The third pulse for creating SBS described in Section 4.1.3 and the third pulse for creating $|\blacktriangle\rangle$ are similar, both by two-photon Rydberg laser excitation of the transitions

$$\begin{aligned}|{\rm g}_\uparrow\rangle &\xrightarrow{\Omega_{{\rm gr}\uparrow}=\Omega_{\rm eff}(1+{\rm e}^{2{\rm i}t\Delta})}|r_+\rangle,\\ |{\rm g}_\downarrow\rangle &\xrightarrow{\Omega_{{\rm cr}\downarrow}=-\Omega_{\rm eff}(1+{\rm e}^{-2{\rm i}t\Delta})}|r_-\rangle,\end{aligned}$$

where the sign difference between the ground-Rydberg Rabi frequencies for the $\uparrow$ and $\downarrow$ states is from the selection rule [37]. Though the Hamiltonians are simple, we would like to show them without using the entangled basis states as in Section 4.1.3. We show the simple Hamiltonians also because we would like to clarify that the Hamiltonians are in a rotating frame defined by the energy of the atomic states, which is why we need the

frame transform described in Appendix B when moving from the discussion of the second pulse to the discussion of the third pulse.

For the input state $|c_\uparrow c_\uparrow\rangle$ which is $e^{i\alpha'}\frac{|r_+c_\uparrow\rangle+|c_\uparrow r_+\rangle}{\sqrt{2}}$ at the beginning of the third pulse, the Hamiltonian is

$$\hat{H}_{\uparrow\uparrow}=\begin{pmatrix} 0 & 0 & \frac{\Omega_{g\uparrow}}{2} & 0 \\ 0 & 0 & 0 & \frac{\Omega_{g\uparrow}}{2} \\ \frac{\Omega_{g\uparrow}^*}{2} & 0 & 0 & 0 \\ 0 & \frac{\Omega_{g\uparrow}^*}{2} & 0 & 0 \end{pmatrix} \tag{C1}$$

in the basis of

$$\{|r_+c_\uparrow\rangle, |c_\uparrow r_+\rangle, |g_\uparrow c_\uparrow\rangle, |c_\uparrow g_\uparrow\rangle\}.$$

For the input state $|c_\downarrow c_\downarrow\rangle$ which is $e^{i(\pi-\alpha')}\frac{|r_-c_\downarrow\rangle+|c_\downarrow r_-\rangle}{\sqrt{2}}$ at the beginning of the third pulse, the Hamiltonian is

$$\hat{H}_{\downarrow\downarrow}=\begin{pmatrix} 0 & 0 & \frac{\Omega_{g\downarrow}}{2} & 0 \\ 0 & 0 & 0 & \frac{\Omega_{g\downarrow}}{2} \\ \frac{\Omega_{g\downarrow}^*}{2} & 0 & 0 & 0 \\ 0 & \frac{\Omega_{g\downarrow}^*}{2} & 0 & 0 \end{pmatrix} \tag{C2}$$

in the basis of

$$\{|r_-c_\downarrow\rangle, |c_\downarrow r_-\rangle, |g_\downarrow c_\downarrow\rangle, |c_\downarrow g_\downarrow\rangle\}.$$

Appendix D: Hamiltonians for creating $|\blacktriangle\rangle$

For the ground-Rydberg transition in the third pulse of the protocol for generating $|\blacktriangle\rangle$, the Hamiltonian is similar to that in Appendix C. Below, we show Hamiltonians for the first and second pulses. For $|c_\uparrow c_\uparrow c_\uparrow\rangle \equiv |ccc\rangle_e \otimes |\uparrow\uparrow\uparrow\rangle_n$, the Hamiltonian is

$$\begin{pmatrix} 3V+3\Delta & \frac{\Omega_{c\uparrow}}{2} & \frac{\Omega_{c\uparrow}}{2} & \frac{\Omega_{c\uparrow}}{2} & 0 & 0 & 0 & 0 \\ \frac{\Omega_{c\uparrow}^*}{2} & V+2\Delta & 0 & 0 & \frac{\Omega_{c\uparrow}}{2} & \frac{\Omega_{c\uparrow}}{2} & 0 & 0 \\ \frac{\Omega_{c\uparrow}^*}{2} & 0 & V+2\Delta & 0 & \frac{\Omega_{c\uparrow}}{2} & 0 & \frac{\Omega_{c\uparrow}}{2} & 0 \\ \frac{\Omega_{c\uparrow}^*}{2} & 0 & 0 & V+2\Delta & 0 & \frac{\Omega_{c\uparrow}}{2} & \frac{\Omega_{c\uparrow}}{2} & 0 \\ 0 & \frac{\Omega_{c\uparrow}^*}{2} & \frac{\Omega_{c\uparrow}^*}{2} & 0 & \Delta & 0 & 0 & \frac{\Omega_{c\uparrow}}{2} \\ 0 & \frac{\Omega_{c\uparrow}^*}{2} & 0 & \frac{\Omega_{c\uparrow}^*}{2} & 0 & \Delta & 0 & \frac{\Omega_{c\uparrow}}{2} \\ 0 & 0 & \frac{\Omega_{c\uparrow}^*}{2} & \frac{\Omega_{c\uparrow}^*}{2} & 0 & 0 & \Delta & \frac{\Omega_{c\uparrow}}{2} \\ 0 & 0 & 0 & 0 & \frac{\Omega_{c\uparrow}^*}{2} & \frac{\Omega_{c\uparrow}^*}{2} & \frac{\Omega_{c\uparrow}^*}{2} & 0 \end{pmatrix} \tag{D1}$$

in the basis of

$$\{|r_+r_+r_+\rangle, |r_+r_+c_\uparrow\rangle, |r_+c_\uparrow r_+\rangle, |c_\uparrow r_+r_+\rangle, |r_+c_\uparrow c_\uparrow\rangle, |c_\uparrow r_+c_\uparrow\rangle, |c_\uparrow c_\uparrow r_+\rangle, |c_\uparrow c_\uparrow c_\uparrow\rangle\}.$$

For $|c_\downarrow c_\downarrow c_\downarrow\rangle \equiv |ccc\rangle_e \otimes |\downarrow\downarrow\downarrow\rangle_n$, the Hamiltonian is similar to Eq. (D1) with the difference that $(\Delta, \Omega_{c\uparrow})$ should be replaced by $(-\Delta, \Omega_{c\downarrow})$. For $|c_\uparrow c_\uparrow c_\downarrow\rangle \equiv |ccc\rangle_e \otimes |\uparrow\uparrow\downarrow\rangle_n$, the Hamiltonian is

$$\begin{pmatrix} 3V+\Delta & \frac{\Omega_{c\downarrow}}{2} & \frac{\Omega_{c\uparrow}}{2} & \frac{\Omega_{c\uparrow}}{2} & 0 & 0 & 0 & 0 \\ \frac{\Omega_{c\downarrow}^*}{2} & V+2\Delta & 0 & 0 & \frac{\Omega_{c\uparrow}}{2} & \frac{\Omega_{c\uparrow}}{2} & 0 & 0 \\ \frac{\Omega_{c\uparrow}^*}{2} & 0 & V & 0 & \frac{\Omega_{c\uparrow}}{2} & 0 & \frac{\Omega_{c\uparrow}}{2} & 0 \\ \frac{\Omega_{c\uparrow}^*}{2} & 0 & 0 & V & 0 & \frac{\Omega_{c\downarrow}}{2} & \frac{\Omega_{c\uparrow}}{2} & 0 \\ 0 & \frac{\Omega_{c\uparrow}^*}{2} & \frac{\Omega_{c\uparrow}^*}{2} & 0 & \Delta & 0 & 0 & \frac{\Omega_{c\uparrow}}{2} \\ 0 & \frac{\Omega_{c\uparrow}^*}{2} & 0 & \frac{\Omega_{c\downarrow}^*}{2} & 0 & \Delta & 0 & \frac{\Omega_{c\uparrow}}{2} \\ 0 & 0 & \frac{\Omega_{c\uparrow}^*}{2} & \frac{\Omega_{c\uparrow}^*}{2} & 0 & 0 & -\Delta & \frac{\Omega_{c\downarrow}}{2} \\ 0 & 0 & 0 & 0 & \frac{\Omega_{c\uparrow}^*}{2} & \frac{\Omega_{c\uparrow}^*}{2} & \frac{\Omega_{c\downarrow}^*}{2} & 0 \end{pmatrix} \tag{D2}$$

in the basis of

$$\{|r_+r_+r_-\rangle, |r_+r_+c_\downarrow\rangle, |r_+c_\uparrow r_-\rangle, |c_\uparrow r_+r_-\rangle, |r_+c_\uparrow c_\downarrow\rangle, |c_\uparrow r_+c_\downarrow\rangle, |c_\uparrow c_\uparrow r_-\rangle, |c_\uparrow c_\uparrow c_\downarrow\rangle\}.$$

The Hamiltonian for $|c_x c_y c_z\rangle$ with only one of x, y, and z being $\downarrow$ is similar to Eq. (D2) by an appropriate basis state arrangement. The Hamiltonian for $|c_\downarrow c_\downarrow c_\uparrow\rangle$ is similar to Eq. (D2) via $\pm\Delta \to \mp\Delta$, $\Omega_{c\uparrow} \to \Omega_{c\downarrow}$, and $\Omega_{c\downarrow} \to \Omega_{c\uparrow}$, and

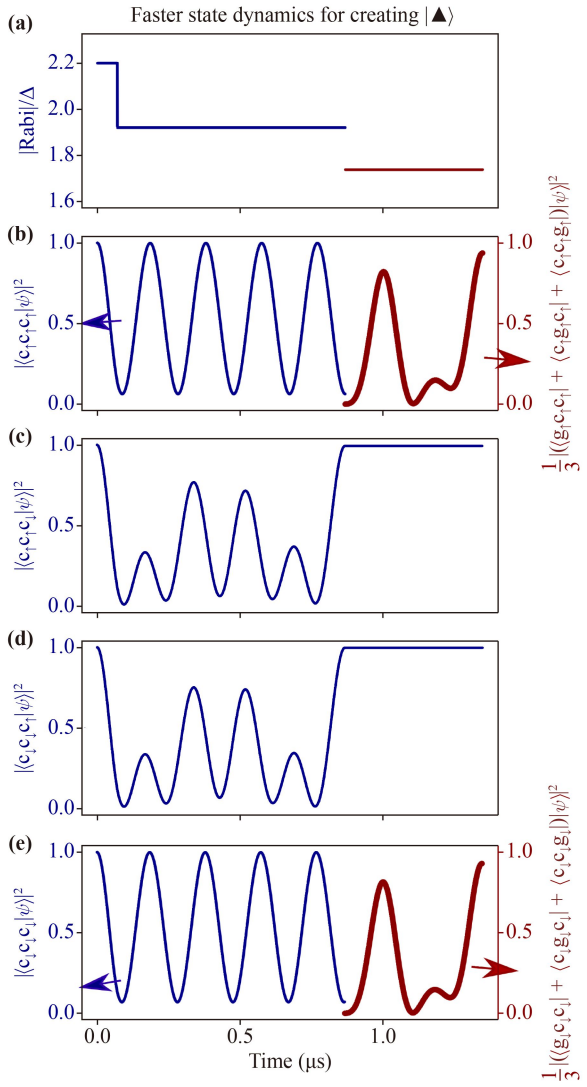

Fig. E1 State dynamics of the $|\blacktriangle\rangle$ protocol with a faster speed with $V_0/(2\pi) = 260$ MHz and maximal Rabi frequency $\Omega^{(\blacktriangle)}/(2\pi) \approx 3.25$ MHz when ignoring Rydberg-state decay. The meaning of the contents are the same as those in Fig. 8. In (b) and (e), there is some population not transferred to the Rydberg state at the end of the second pulse, which results in a larger error of the entanglement generation compared to the case described around Fig. 8.

the Hamiltonian for $|c_x c_y c_z\rangle$ with only one of x, y, and z being $\uparrow$ is similar to the Hamiltonian of $|c_\downarrow c_\downarrow c_\uparrow\rangle$.

For the input state $|c_\uparrow c_\uparrow c_\uparrow\rangle$ which is $\frac{e^{i\alpha^{(\blacktriangle)'}}}{\sqrt{3}}(|r_+ c_\uparrow c_\uparrow\rangle + |c_\uparrow r_+ c_\uparrow\rangle + |c_\uparrow c_\uparrow r_+\rangle)$ at the beginning of the third pulse, the Hamiltonian is a 6×6 matrix written in the basis of $\{|r_+ c_\uparrow c_\uparrow\rangle, |c_\uparrow r_+ c_\uparrow\rangle, |c_\uparrow c_\uparrow r_+\rangle, |g_\uparrow c_\uparrow c_\uparrow\rangle, |c_\uparrow g_\uparrow c_\uparrow\rangle, |c_\uparrow c_\uparrow\rangle g_\uparrow\}$ in which three pairs of states are coupled in a way similar to that of Eq. (C1). For the input state $|c_\downarrow c_\downarrow c_\downarrow\rangle$ which is $\frac{e^{-i\alpha^{(\blacktriangle)'}}}{\sqrt{3}}(|r_- c_\downarrow c_\downarrow\rangle + |c_\downarrow r_- c_\downarrow\rangle + |c_\downarrow c_\downarrow r_-\rangle)$ at the beginning of the third pulse, the Hamiltonian is written in a way similar to that in Eq. (C2) in an appropriate six-ket basis.

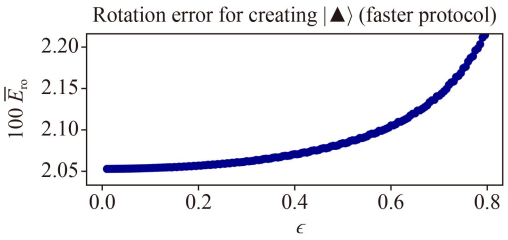

Fig. E2 Rotation error (scaled by 100) averaged by uniformly varying the Rydberg interaction V in $[(1-\epsilon)V_0,\ (1+\epsilon)V_0]$ for creating $|\blacktriangle\rangle$ with the parameters of Fig. E1 and Appendix E. The fidelity to generate $|\blacktriangle\rangle$ in the form similar to that in Eq. (33), $1-\overline{E}_{ro}-E_{decay}$, is about 0.972 for $\epsilon = 0.8$.

Appendix E: A faster protocol for creating $|\blacktriangle\rangle$

The protocols in Sections 2, 3, and 4 describe high-fidelity methods. Sometimes a fast entangling gate is helpful for certain purposes. One approach to faster entanglement is to find approximate excitation of Rydberg states. We take the generation of $|\blacktriangle\rangle$ as an example. In Section 4, the first pulse has a long duration so as to have a high-fidelity generation of the Rydberg states in Eq. (28). One can use a shorter pulse to achieve it though the fidelity is a little lower. We find that with the three Rabi frequencies equal to $(2.2, 1.92, 1.737)\Delta$ and the three pulse durations $(0.206, 2.36, 1.421)\pi/\Delta$, we can approximately realize the state $|\blacktriangle\rangle$ with a total duration $8.8\pi/\Omega_m$, where Ω_m is the maximal Rabi frequency (of the first pulse). With these parameters and the same maximal Rabi frequency used in Fig. 8, we simulate the state dynamics, and found that the final populations are 0.937, 0.993, 0.997, and 0.929 respectively for the four typical types of input states $|c_\uparrow c_\uparrow c_\uparrow\rangle, |c_\uparrow c_\uparrow c_\downarrow\rangle, |c_\downarrow c_\downarrow c_\uparrow\rangle, |c_\downarrow c_\downarrow c_\downarrow\rangle$, shown in Fig. E1. The Rydberg-state decay induces an error $E_{decay} \approx 1.79\pi/(\tau\Delta)$, which is about 6.06×10^{-3} when $\Omega^{(\blacktriangle)}/(2\pi) \approx 3.25$ MHz and $\tau = 100$ μs. For this case, the main error in the entanglement generation is the population loss which can be obviously seen in Figs. E1(b) and (d), which leads to large rotation errors as shown in Fig. E2. With a large interaction fluctuation ratio $\epsilon = 0.8$, the fidelity is about 0.972 for generating the target state. We would like to point out that by pulse shaping techniques [18, 47] one can in principle design much faster protocols with high fidelity, but our purpose is to show that the near degeneracy of the nuclear spin qubits in a weak magnetic field can enable fast generation of exotic entanglement between nuclear spins and electrons in multiple atoms.

References

1. D. Jaksch, J. I. Cirac, P. Zoller, S. L. Rolston, R. Cote,

and M. D. Lukin, Fast quantum gates for neutral atoms, *Phys. Rev. Lett.* 85(10), 2208 (2000)
2. M. D. Lukin, M. Fleischhauer, R. Cote, L. M. Duan, D. Jaksch, J. I. Cirac, and P. Zoller, Dipole blockade and quantum information processing in mesoscopic atomic ensembles, *Phys. Rev. Lett.* 87(3), 037901 (2001)
3. T. Wilk, A. Gaetan, C. Evellin, J. Wolters, Y. Miroshnychenko, P. Grangier, and A. Browaeys, Entanglement of two individual neutral atoms using Rydberg blockade, *Phys. Rev. Lett.* 104(1), 010502 (2010)
4. L. Isenhower, E. Urban, X. L. Zhang, A. T. Gill, T. Henage, T. A. Johnson, T. G. Walker, and M. Saffman, Demonstration of a neutral atom controlled-NOT quantum gate, *Phys. Rev. Lett.* 104(1), 010503 (2010)
5. X. L. Zhang, L. Isenhower, A. T. Gill, T. G. Walker, and M. Saffman, Deterministic entanglement of two neutral atoms via Rydberg blockade, *Phys. Rev. A* 82, 030306(R) (2010)
6. K. M. Maller, M. T. Lichtman, T. Xia, Y. Sun, M. J. Piotrowicz, A. W. Carr, L. Isenhower, and M. Saffman, Rydberg-blockade controlled-not gate and entanglement in a two-dimensional array of neutral-atom qubits, *Phys. Rev. A* 92(2), 022336 (2015)
7. Y. Y. Jau, A. M. Hankin, T. Keating, I. H. Deutsch, and G. W. Biedermann, Entangling atomic spins with a Rydberg-dressed spin-flip blockade, *Nat. Phys.* 12(1), 71 (2016)
8. Y. Zeng, P. Xu, X. He, Y. Liu, M. Liu, J. Wang, D. J. Papoular, G. V. Shlyapnikov, and M. Zhan, Entangling two individual atoms of different isotopes via Rydberg blockade, *Phys. Rev. Lett.* 119(16), 160502 (2017)
9. H. Levine, A. Keesling, A. Omran, H. Bernien, S. Schwartz, A. S. Zibrov, M. Endres, M. Greiner, V. Vuletíc, and M. D. Lukin, High-fidelity control and entanglement of Rydberg atom qubits, *Phys. Rev. Lett.* 121(12), 123603 (2018)
10. C. J. Picken, R. Legaie, K. McDonnell, and J. D. Pritchard, Entanglement of neutral-atom qubits with long ground-Rydberg coherence times, *Quantum Sci. Technol.* 4(1), 015011 (2018)
11. H. Levine, A. Keesling, G. Semeghini, A. Omran, T. T. Wang, S. Ebadi, H. Bernien, M. Greiner, V. Vuletíc, H. Pichler, and M. D. Lukin, Parallel implementation of high-fidelity multi-qubit gates with neutral atoms, *Phys. Rev. Lett.* 123(17), 170503 (2019)
12. T. M. Graham, M. Kwon, B. Grinkemeyer, Z. Marra, X. Jiang, M. T. Lichtman, Y. Sun, M. Ebert, and M. Saffman, Rydberg mediated entanglement in a two-dimensional neutral atom qubit array, *Phys. Rev. Lett.* 123(23), 230501 (2019)
13. H. Jo, Y. Song, M. Kim, and J. Ahn, Rydberg atom entanglements in the weak coupling regime, *Phys. Rev. Lett.* 124(3), 033603 (2020)
14. Z. Fu, P. Xu, Y. Sun, Y. Y. Liu, X. D. He, X. Li, M. Liu, R. B. Li, J. Wang, L. Liu, and M. S. Zhan, High-fidelity entanglement of neutral atoms via a Rydberg-mediated single-modulated-pulse controlled-PHASE gate, *Phys. Rev. A* 105(4), 042430 (2022)
15. K. McDonnell, L. F. Keary, and J. D. Pritchard, Demonstration of a quantum gate using electromagnetically induced transparency, *Phys. Rev. Lett.* 129(20), 200501 (2022)
16. D. Bluvstein, H. Levine, G. Semeghini, T. T. Wang, S. Ebadi, M. Kalinowski, A. Keesling, N. Maskara, H. Pichler, M. Greiner, V. Vuleti'c, and M. D. Lukin, A quantum processor based on coherent transport of entangled atom arrays, *Nature* 604(7906), 451 (2022)
17. T. M. Graham, Y. Song, J. Scott, C. Poole, L. Phuttitarn, K. Jooya, P. Eichler, X. Jiang, A. Marra, B. Grinkemeyer, M. Kwon, M. Ebert, J. Cherek, M. T. Lichtman, M. Gillette, J. Gilbert, D. Bowman, T. Ballance, C. Campbell, E. D. Dahl, O. Crawford, N. S. Blunt, B. Rogers, T. Noel, and M. Saffman, Multi-qubit entanglement and algorithms on a neutral-atom quantum computer, *Nature* 604(7906), 457 (2022)
18. S. J. Evered, D. Bluvstein, M. Kalinowski, S. Ebadi, T. Manovitz, H. Zhou, S. H. Li, A. A. Geim, T. T. Wang, N. Maskara, H. Levine, G. Semeghini, M. Greiner, V. Vuletic, and M. D. Lukin, High-fidelity parallel entangling gates on a neutral atom quantum computer, arXiv: 2304.05420v1 (2023)
19. I. S. Madjarov, J. P. Covey, A. L. Shaw, J. Choi, A. Kale, A. Cooper, H. Pichler, V. Schkolnik, J. R. Williams, and M. Endres, High-fidelity entanglement and detection of alkaline-earth Rydberg atoms, *Nat. Phys.* 16(8), 857 (2020)
20. S. Ma, A. P. Burgers, G. Liu, J. Wilson, B. Zhang, and J. D. Thompson, Universal gate operations on nuclear spin qubits in an optical tweezer array of ^{171}Yb atoms, *Phys. Rev. X* 12(2), 021028 (2022)
21. N. Schine, A. W. Young, W. J. Eckner, M. J. Martin, and A. M. Kaufman, Long-lived Bell states in an array of optical clock qubits, *Nat. Phys.* 18(9), 1067 (2022)
22. P. Scholl, A. L. Shaw, R. B. S. Tsai, R. Finkelstein, J. Choi, and M. Endres, Erasure conversion in a high-fidelity Rydberg quantum simulator, arXiv: 2305.03406v1 (2023)
23. S. Ma, G. Liu, P. Peng, B. Zhang, S. Jandura, A. P. Burgers, G. Pupillo, S. Puri, and J. D. Thompson, High-fidelity gates with mid-circuit erasure conversion in a metastable neutral atom qubit, arXiv: 2305.05493v1 (2023)
24. R. Yamamoto, J. Kobayashi, T. Kuno, K. Kato, and Y. Takahashi, An ytterbium quantum gas microscope with narrow-line laser cooling, *New J. Phys.* 18(2), 023016 (2016)
25. S. Saskin, J. T. Wilson, B. Grinkemeyer, and J. D. Thompson, Narrow-line cooling and imaging of ytterbium atoms in an optical tweezer array, *Phys. Rev. Lett.* 122(14), 143002 (2019)
26. A. Cooper, J. P. Covey, I. S. Madjarov, S. G. Porsev, M. S. Safronova, and M. Endres, Alkaline-earth atoms in optical tweezers, *Phys. Rev. X* 8(4), 041055 (2018)
27. M. A. Norcia, A. W. Young, and A. M. Kaufman, Microscopic control and detection of ultracold strontium in optical-tweezer arrays, *Phys. Rev. X* 8(4), 041054 (2018)
28. J. P. Covey, I. S. Madjarov, A. Cooper, and M. Endres, 2000-times repeated imaging of strontium atoms in clock-magic tweezer arrays, *Phys. Rev. Lett.* 122(17), 173201 (2019)
29. J. T. Wilson, S. Saskin, Y. Meng, S. Ma, R. Dilip, A. P.

Burgers, and J. D. Thompson, Trapping alkaline earth Rydberg atoms optical tweezer arrays, *Phys. Rev. Lett.* 128(3), 033201 (2022)
30. A. J. Daley, M. M. Boyd, J. Ye, and P. Zoller, Quantum computing with alkaline-earth-metal atoms, *Phys. Rev. Lett.* 101(17), 170504 (2008)
31. A. V. Gorshkov, A. M. Rey, A. J. Daley, M. M. Boyd, J. Ye, P. Zoller, and M. D. Lukin, Alkaline-earth-metal atoms as few-qubit quantum registers, *Phys. Rev. Lett.* 102(11), 110503 (2009)
32. I. Reichenbach and I. H. Deutsch, Sideband cooling while preserving coherences in the nuclear spin state in group-II-like atoms, *Phys. Rev. Lett.* 99(12), 123001 (2007)
33. X. F. Shi, Coherence-preserving cooling of nuclear-spin qubits in a weak magnetic field, *Phys. Rev. A* 107(2), 023102 (2023)
34. S. Omanakuttan, A. Mitra, M. J. Martin, and I. H. Deutsch, Quantum optimal control of ten-level nuclear spin qudits in ^{87}Sr, *Phys. Rev. A* 104(6), L060401 (2021)
35. N. Chen, L. Li, W. Huie, M. Zhao, I. Vetter, C. H. Greene, and J. P. Covey, Analyzing the Rydberg-based optical-metastable-ground architecture for ^{171}Yb nuclear spins, *Phys. Rev. A* 105(5), 052438 (2022)
36. M. M. Boyd, T. Zelevinsky, A. D. Ludlow, S. Blatt, T. Zanon-Willette, S. M. Foreman, and J. Ye, Nuclear spin effects in optical lattice clocks, *Phys. Rev. A* 76(2), 022510 (2007)
37. X. F. Shi, Rydberg quantum computation with nuclear spins in two-electron neutral atoms, *Front. Phys.* 16(5), 52501 (2021)
38. X. F. Shi, Fast, accurate, and realizable two-qubit entangling gates by quantum interference in detuned Rabi cycles of Rydberg atoms, *Phys. Rev. Appl.* 11(4), 044035 (2019)
39. K. Barnes, P. Battaglino, B. J. Bloom, K. Cassella, N. Coxe, N. Crisosto, J. P. King, S. S. Kondov, K. Kotru, S. C. Larsen, J. Lauigan, B. J. Lester, M. McDonald, E. Megidish, S. Narayanaswami, C. Nishiguchi, R. Notermans, L. S. Peng, A. Ryou, T. Y. Wu, and M. Yarwood, Assembly and coherent control of a register of nuclear spin qubits, *Nat. Commun.* 13(1), 2779 (2022)
40. A. Jenkins, J. W. Lis, A. Senoo, W. F. McGrew, and A. M. Kaufman, Ytterbium nuclear-spin qubits in an optical tweezer array, *Phys. Rev. X* 12(2), 021027 (2022)
41. C. H. Bennett and S. J. Wiesner, Communication via one- and two-particle operators on Einstein–Podolsky–Rosen states, *Phys. Rev. Lett.* 69(20), 2881 (1992)
42. W. Dür, G. Vidal, and J. I. Cirac, Three qubits can be entangled in two inequivalent ways, *Phys. Rev. A* 62(6), 062314 (2000)
43. B. Fang, M. Menotti, M. Liscidini, J. E. Sipe, and V. O. Lorenz, Three-photon discrete-energy-entangled W state in an optical fiber, *Phys. Rev. Lett.* 123(7), 070508 (2019)
44. D. M. Greenberger, M. Horne, and A. Zeilinger, Bell's Theorem, Quantum Theory, and Conceptions of the Universe, edited by M. Kafatos, Kluwer, Dordrecht, 1989
45. X. F. Shi, Hyperentanglement of divalent neutral atoms by Rydberg blockade, *Phys. Rev. A* 104(4), 042422 (2021)
46. M. Saffman, T. G. Walker, and K. Mølmer, Quantum information with Rydberg atoms, *Rev. Mod. Phys.* 82(3), 2313 (2010)
47. X. F. Shi, Quantum logic and entanglement by neutral Rydberg atoms: Methods and fidelity, *Quantum Sci. Technol.* 7(2), 023002 (2022)
48. A. P. Burgers, S. Ma, S. Saskin, J. Wilson, M. A. Alarcón, C. H. Greene, and J. D. Thompson, Controlling Rydberg excitations using ion core transitions in alkaline earth atom tweezer arrays, *PRX Quantum* 3(2), 020326 (2022)
49. R. Ding, J. D. Whalen, S. K. Kanungo, T. C. Killian, F. B. Dunning, S. Yoshida, and J. Burgdörfer, Spectroscopy of ^{87}Sr triplet Rydberg states, *Phys. Rev. A* 98(4), 042505 (2018)
50. A. Lurio, M. Mandel, and R. Novick, Second-order hyperfine and Zeeman corrections for an (sl) configuration, *Phys. Rev.* 126(5), 1758 (1962)
51. X. F. Shi, Rydberg quantum gates free from blockade error, *Phys. Rev. Appl.* 7(6), 064017 (2017)
52. X. F. Shi, Accurate quantum logic gates by spin echo in Rydberg atoms, *Phys. Rev. Appl.* 10(3), 034006 (2018)
53. C. P. Williams, Explorations in Quantum Computing, 2nd Ed., edited by D. Gries and F. B. Schneider, Texts in Computer Science, Springer-Verlag, London, 2011
54. M. Saffman and T. G. Walker, Analysis of a quantum logic device based on dipole–dipole interactions of optically trapped Rydberg atoms, *Phys. Rev. A* 72(2), 022347 (2005)
55. L. H. Pedersen, N. M. Møller, and K. Mølmer, Fidelity of quantum operations, *Phys. Lett. A* 367(1–2), 47 (2007)
56. X. F. Shi, Deutsch, Toffoli, and CNOT gates via rydberg blockade of neutral atoms, *Phys. Rev. Appl.* 9, 051001(R) (2018)
57. X. F. Shi, Transition slow-down by Rydberg interaction of neutral atoms and a fast controlled-NOT quantum gate, *Phys. Rev. Appl.* 14(5), 054058 (2020)
58. J. L. Wu, Y. Wang, J. X. Han, S. L. Su, Y. Xia, Y. Jiang, and J. Song, Unselective ground-state blockade of Rydberg atoms for implementing quantum gates, *Front. Phys.* 17(2), 22501 (2022)
59. S. Liu, J. H. Shen, R. H. Zheng, Y. H. Kang, Z. C. Shi, J. Song, and Y. Xia, Optimized nonadiabatic holonomic quantum computation based on Förster resonance in Rydberg atoms, *Front. Phys.* 17(2), 21502 (2022)
60. V. M. Stojanović and J. K. Nauth, Interconversion of W and Greenberger–Horne–Zeilinger states for Ising-coupled qubits with transverse global control, *Phys. Rev. A* 106(5), 052613 (2022)
61. X. Wu, X. Liang, Y. Tian, F. Yang, C. Chen, Y. C. Liu, M. K. Tey, and L. You, A concise review of Rydberg atom based quantum computation and quantum simulation, *Chin. Phys. B* 30(2), 020305 (2021)
62. D. R. Chong, M. Kim, J. Ahn, and H. Jeong, Machine learning identification of symmetrized base states of Rydberg atoms, *Front. Phys.* 17(1), 12504 (2022)
63. H. Zhang, J. Wu, M. Artoni, and G. C. La Rocca, Single-photon-level light storage with distributed Rydberg excitations in cold atoms, *Front. Phys.* 17(2),

22502 (2022)
64. J. P. Covey, A. Sipahigil, S. Szoke, N. Sinclair, M. Endres, and O. Painter, Telecom-band quantum optics with ytterbium atoms and silicon nanophotonics, *Phys. Rev. Appl.* 11(3), 034044 (2019)
65. A. D. Boozer, A. Boca, R. Miller, T. E. Northup, and H. J. Kimble, Reversible state transfer between light and a single trapped atom, *Phys. Rev. Lett.* 98(19), 193601 (2007)
66. Y. Wu, S. Kolkowitz, S. Puri, and J. D. Thompson, Erasure conversion for fault-tolerant quantum computing in alkaline earth Rydberg atom arrays, *Nat. Commun.* 13(1), 4657 (2022)
67. A. Mitra, M. J. Martin, G. W. Biedermann, A. M. Marino, P. M. Poggi, and I. H. Deutsch, Robust Mølmer–Sørensen gate for neutral atoms using rapid adiabatic Rydberg dressing, *Phys. Rev. A* 101, 030301(R) (2020)
68. K. L. Pham, T. F. Gallagher, P. Pillet, S. Lepoutre, and P. Cheinet, A coherent light shift on alkaline-earth Rydberg atoms from isolated core excitation without auto-ionization, *PRX Quantum* 3(2), 020327 (2022)